

Microstructural origins of the high mechanical damage tolerance of NbTaMoW refractory high-entropy alloy thin films

Matheus A. Tunes^{a,1,*}, Vladimir M. Vishnyakov^{a,*}

^a*Institute for Materials Research, University of Huddersfield, Queensgate, HD1 3DH, United Kingdom*

Abstract

Refractory NbTaMoW thin films in close to equiatomic composition were deposited by ion beam sputter-deposition at room temperature. Energy-filtered transmission electron microscopy shows uniform distribution of all elements and electron diffraction patterns reveals unvarying body-centred cubic crystalline structure. Transmission electron microscopy images show large grains with columnar morphology. Argon bubbles with around 1.3 ± 0.4 nm diameter were witnessed. The film growth mechanisms are discussed based on high-entropy film nature, general nucleation and growth theory and the Movchan-Demchishin-Thornton structure-zone growth models. Nanoindentation showed that the films have hardness of 22.8 ± 0.7 GPa. Nanoscratching demonstrated that the film high hardness is also connected with high crack and delamination resistances. This indicates high mechanical damage tolerance (*e.g.* toughness). The results show that the combination of refractory metals with the intrinsic characteristics of high-entropy alloy systems in the NbTaMoW case can be considered as a hard coating candidate for future application in extreme environments.

Keywords: Thin Films, Refractory High-Entropy Alloys, Transmission Electron Microscopy, Energy Filtered Transmission Electron Microscopy, Nanoindentation, Nanoscratching

Highlights

- A Nb₂₃Ta₂₃Mo₂₉W₂₅ high-entropy alloy thin film was ion beam sputter-deposited.
- The film has body-centred cubic structure and columnar grain morphology.
- As-deposited film has hardness of 22.8 GPa and high crack and delamination resistances.
- The film toughness is based on the refractory and high-entropy natures and by dislocation pinning by Ar bubbles.

*Corresponding authors:

Email addresses: matheus.tunes@unileoben.ac.at (Matheus A. Tunes), v.vishnyakov@hud.ac.uk (Vladimir M. Vishnyakov)

¹Present address: Chair of non-ferrous metallurgy, Montanuniversitaet Leoben, Franz-Josef-Straße 18, A-8700 Leoben, Austria.

1. Introduction

Refractory materials and alloys are of paramount importance for the modern industry. Applications such as aerospace vehicles, innovative nuclear power reactors designs, aircraft turbines and several different types of manufacturing parts have to meet the requirements and the engineering criteria of operating at elevated temperatures in harmful environmental conditions. Within this context, as general guidelines for materials selection and design, new prospective refractory ceramic compounds and metallic alloys are expected to exhibit superior ultra high-temperature oxidation and corrosion resistances, long-term microstructural stability and superior mechanical strength and creep resistance over complexes temperature gradients when compared with existing Ni superalloys and conventional refractory ceramics [1–10].

Recently, the advent of high-entropy alloys (HEAs) has shed light on a possibility of designing new metallic multicomponent alloys with improved properties when compared with conventional alloy systems [11, 12]. HEAs are a complex class of concentrated solid solution alloys (CSAs) with five or more elements that are produced by combining different elements, but at (nearly) equiatomic proportions. Alloys based on a single principal element are known as low-entropy alloys as well as those from two to four principal elements are sometimes referred to either medium-entropy alloys or high-entropy alloys [13, 14]. As the mixing rule dictates alloying elements with different atomic sizes and at equal molar proportions, the crystalline structure is a random solid solution: a concept that deviates from classical terminal solid solution concept in metallurgy. This specific elemental composition rule confers to the HEAs high thermodynamic stability, good mechanical properties, improved oxidation and corrosion resistances and high damage tolerance upon exposure to energetic particle irradiation [15–21]. Nevertheless, the possibility of alloying refractory metals (such as Nb, W, Ta and Mo) in a form of high-entropy alloys would result in an entire new class of composition-tuneable highly-concentrated multicomponent alloys that preserves the unique mentioned properties of HEAs with high-melting points: the refractory high-entropy alloys (RHEAs) [22–27]. In addition to the refractory property, recent reports on the relationship between unique microstructure and mechanical properties shed light on the possibility of design new metallic alloys with superior damage tolerance [28–33].

To date, a considerable number of RHEAs systems have been explored [23], but the NbTaMoW and NbTaMoWV RHEAs were primarily investigated by Senkov *et al.* [22]. The alloys, produced by the vacuum arc melting technique, were characterised by X-Ray Diffraction (XRD) and exhibited body-centred cubic (BCC) structure, densities of $14 \text{ g}\cdot\text{cm}^{-3}$ and relatively high hardness for a metallic alloy, around of 5 GPa. Further examination indicated that these bulk alloys preserved the random solid solution after annealing at 1673 K, although some elastic parameters, such as the yield strength, have considerably decreased upon increasing the temperature [34].

Regarding HEAs on general, different systems have been also explored. The oxidation resistance of the NbCrMoTi and NbCrMoV quaternary systems with small additions of Al and Si was studied by Liu *et al.* [35]. The authors reported on the overall deleterious effect of the Al addition in terms of degrading the oxidation resistance. However, Si and Ti additions were reported to improve the oxidation resistance. On the other hand, the addition of Al into the system MoNbTaTiZr was reported

by Senkov *et al.* to improve the mechanical properties of the alloy [36]. Reduced contents of Mo and V (deviating from the equiatomic condition) within a different alloy, TiZrNbMoV, was found to increase its single phase (BCC) stability [37]. The HfMoTaTiZr/HfMoNbTaTiZr and MoAlWCrTi RHEAs have also been produced by Juan *et al.* [38] and Garr *et al.* [39], respectively, and have exhibited similar results to the previous RHEAs systems. Recently, Anzorena *et al.* produced and characterised the novel quinary refractory MoTaVWZr high-entropy alloy which showed hardness in excess of 6.7 GPa and potential high radiation resistance [40]. It is worth emphasising that all these bulk RHEAs alloys were of large equiaxed crystal grains and, up to date, the NbTaMoW/NbTaMoWV systems are the most studied RHEAs [22, 41].

As opposed to bulk metallic RHEAs approach, the present challenge is to produce refractory high-entropy alloy thin films (RHEATFs) that could be applied as coatings onto conventional metallic alloys substrates aiming at to increase their applicability in extreme environments. Main motivations lie in the fact that to replace conventional alloys with bulk HEAs or RHEAs would be an expensive task if the costs and natural availability of some refractory metals are taken into consideration. These RHEATFs could be used as coating in existing metallic alloys, thus delivering the desired properties to an engineering item surface. Recently, HEATFs have been extensively studied [42–46] and their mechanical properties were compared with arc-melted bulk HEAs by Gorban *et al.* [47]: the prominent increase in hardness of the thin films when compared with the bulk synthesised alloys was attributed to the nanocrystalline nature of the HEATFs. The feasibility of depositing high-entropy alloy thin films was also recently explored by our group, studying a the FeCrMnNi system [48] and the thin film was demonstrated to be a suitable candidate material for applications within the context of nuclear technology.

In this paper, we report an ion beam sputter-deposition (IBSD) in-depth investigation of the synthesis of the NbTaMoW refractory high-entropy alloy thin film. Post-deposition characterisation were carried out using conventional transmission electron microscopy (TEM) and analytical energy-filtered transmission electron microscopy (EFTEM) techniques. The produced thin films were studied at two conditions: as-deposited and after extended annealing in-air at 523 K. Mechanical properties were measured using nanoindentation and nanoscratching techniques which allowed the investigation of the mechanical damage tolerance of the RHEATF [49]. Results, properties and prospects for the synthesis and application of such RHEATFs are discussed and based on previous reports on the multicomponent NbTaMoW system as well as the current understanding on the metallurgy of highly-concentrated multicomponent alloy systems.

2. Materials and methods

Thin solid films from the system NbTaMoW were produced using the ion beam sputter-deposition (IBSD) technique. An Ar ion beam with energy of 1.25 keV was used to sputter the elemental targets onto a electronic-grade silicon wafer substrate that was chosen for the purposes of developing understanding of fundamental processes. The base pressure in the deposition chamber was measured to be 1.5×10^{-4} Pa and at around of 2×10^{-2} Pa (Ar partial pressure) during the film deposition. The deposition was carried out during 2 hours without any additional substrate heating. Throughout the

deposition, the substrate temperature increased to around 370–400 K. Detailed description of the IBSD system can be found in previously published works [48, 50].

As the elemental composition of the thin film product is directly related to the geometric position of the sputtering targets with respect to the Ar ion beam, the elemental Nb, Ta, Mo and W target areas were geometrically adjusted under the ion beam to achieve the desired elemental composition [48]. An FEI Quanta 3D FEG scanning electron microscope (SEM) equipped with an Oxford Instruments energy dispersive X-ray (EDX) spectroscopy detector was used to record the X-Ray spectra. The standardless ZAF correction method [51] was used for data quantification and the elemental composition of the RHEATF. Aiming at to analyse the stability and the behaviour of coating elements at moderate temperatures, part of the coated Si substrate was annealed at around 523 ± 5 K during 10 hours in-air on a hot plate. This temperature was chosen to promote diffusion of punctual defects without significantly inducing Si diffusion from the substrate to the film.

Conventional focused ion beam (FIB) technique [52] was used to prepare electron transparent samples of the RHEATF in the as-deposited and in-air annealed conditions. For the TEM specimen preparation, a FEI Quanta 200 3D SEM-FIB operating with Ga^+ ions was used. A Hitachi H-9500 Transmission Electron Microscope was employed to characterise the microstructure of the thin films by means of conventional techniques such as bright- and dark-field (BFTEM and DFTEM) as well as to record selected-area diffraction pattern (SAED). The TEM is equipped with an analytical Gatan Quantum SE spectrometer that was used for EFTEM. The energy resolution of the system was around of 2.2 eV at 300 keV and an energy slit of 20 eV was used for the elemental map acquisition. ImageJ software was used for analysis of the TEM images and quantification of the thin film defects [53].

Micro Materials nanomechanics platform was used to measure the films hardness and to perform nanoscratching tests. Berkovich nanoindenter (3-sided diamond pyramid with 65.3° corner) calibrated on silica and tungsten was used for the nanoindentation measurements. These measurements were carried out with the loads from 1 to 10 mN which allowed penetration to the maximum depth of 80 nm. The loads were chosen to avoid surface hardness uncertainties and to penetrate the films below 10% of the thickness. The nanoscratching was performed with worn Berkovich indenter by ramping load from 0 to 500 mN while scanning sample for $500\ \mu\text{m}$. In order to compare the nanostraching behaviour of the RHEATF, titanium nitride (TiN) thin films were used. These films were deposited under similar conditions (*i.e.* deposition parameters) to the RHEATF, except the nitrogen which is added to the chamber for reactive deposition: detailed information can be on the synthesis of TiN thin films can be found elsewhere [54]. Different indenters were used for either nanoscratching and nanoindentation.

3. Results

After deposition, the thickness of the RHEATF was measured in the SEM-FIB to be around of $2.0\pm 0.2\ \mu\text{m}$ and the elemental composition of the RHEATF as-deposited is shown at the table 1. Assuming the nominal density of the coating elements (table 2), the calculated density of the produced RHEATF is $13.6\ \text{g}\cdot\text{cm}^{-3}$.

TEM analysis of the thin film before annealing has revealed a columnar grain structure with sizes

around of 100-200 nm as shown in both BFTEM and DFTEM micrographs in the figure 1. The underfocused BFTEM micrograph in the figure 1(b) exhibited the presence of small round features with an average diameter size of 1.3-1.5 nm. Additionally, the DFTEM micrographs 1(c) and 1(e) showed small black-spots that were observable with the $[1\bar{1}0]$ reflection. Indexing of the diffraction patterns has been performed with reference data available in the literature [55, 56] and confirmed that the thin film is of body-centred cubic structure.

Qualitative EFTEM analysis of the thin film before annealing shows that the alloying elements Mo and Ta were uniformly distributed along in film profile as exhibited in figure 2. W and Nb exhibited slightly depleted or enriched regions following the columnar aspect of the thin film. This is attributed to electron-loss signal differences in areas with different electron-transparent thicknesses. Argon was observed to be slightly accumulated at the interface between the film and the Si substrate. O was observed only at the **edge** of the thin film and C was distributed along the thin film with, substrate as well as accumulated at the interface.

The microstructure of the RHEATF after in-air annealing in a hot plate is showed in the figure 3. The BFTEM and DFTEM micrographs 3(a-b) show that both columnar grain morphology and crystal structure were preserved. One particular feature observed in the thin film after annealing was the accumulation of round particles at the grain boundaries with sizes as low as 1.2 nm and as high as 2 nm, as can be observed in the underfocused BFTEM micrograph in the figure 3(c). EFTEM analysis revealed that Ta, Mo and W have migrated to the interface between with the Si substrate as shown in the figure 4. At these conditions, O was also detected **in very low concentration** along the thin film profile and the Si substrate.

With the diffraction patterns, it was possible to estimate the lattice parameters of the thin films. For the thin film before annealing, the lattice parameters were 2.96, 2.93 and 2.93 Å, associated with the reflections $[\bar{1}01]$, $[\bar{1}10]$ and $[01\bar{1}]$, respectively. After annealing, the lattice parameters were observed to increase slightly to: 3.19, 3.19 and 3.06 Å, respectively for the same reflections above. The small round particles observed in the underfocused micrographs are bubbles filled with argon. The bubble diameter distributions before and after annealing are presented in the figure 5.

Nanoindentation measurements of the thin films as-deposited and after annealing allowed the estimation of both hardness and reduced Young's modulus. Figure 6(a) shows that the thin film as-deposited has hardness around 22.8 ± 0.7 GPa while for the annealed, the hardness has dropped to around 16.0 ± 0.6 GPa. At the same time, the reduced Young modulus for the film before annealing was estimated to be approximately 286.6 ± 5.8 GPa as opposed to 236.9 ± 7.1 GPa after annealing. Both hardness and Young modulus are constant in depth which indicates the absence of tip geometric effects and surface/substrate influence within used nanoindentation load range. Nanoscratching was performed with an old Berkovich indenter and the load was linearly ramped within the scratch distance up to maximum load of 500 mN. As the RHEATF exhibited high hardness which is comparable with conventional TiN ceramic coating (hardness of 25.4 GPa, reduced Young's modulus of 321.3 GPa [54] and same thickness as the RHEATF), nanoscratching measurements were performed in both materials (as-deposited) under same experimental conditions. The SEM micrographs in the figure 7 show results obtained with nanoscratching for either RHEATF and TiN: the traces in the micrograph

7(b) show that the TiN is more prone to crack in an uncontrolled manner when compared to the RHEATF in the micrograph 7(a).

4. Discussion

4.1. Relationships between sputter-deposition and the microstructures

It is well established in the thin film deposition community that the microstructure of sputter-deposited hard coatings depends on the system parameters during the deposition stages. Among the wide variety of parameters, the homologous temperature (T/T_m where T is the deposition temperature and T_m is the material's melting point) plays a key role on the final grain structure morphology as it is directly associated with the atomic diffusion of coating species during the deposition stages [57]. The rule of mixing can be used to reasonable estimate the melting point of the produced NbTaMoW RHEATF [34]. Using the melting points of each refractory metals, presented at table 2, the T_m for the thin film was estimated to be approximately 3177 K. With the known substrate temperature during the deposition, the homologous temperature for the deposition of the NbTaMoW RHEATF in this work has been calculated: $T/T_m=0.13$.

The grain morphology herein reported for the RHEATF, as revealed by the BFTEM and DFTEM analysis, consisted of large columnar grains. These observations can be analysed by two major processes that govern the relationships between crystal grain morphology and the IBSD technique. The first is associated with the directionally of the flux of coating species towards the substrate which is a particular aspect of the IBSD technique [57]. The second is due to the low homologous temperature during deposition, in this present case, $T=0.13T_m$. According to the structure-zone model proposed by Movchan and Demchishin (MD) [58], for homologous temperatures lower than $0.3T_m$, a columnar microstructure is expected as a consequence of the low atomic mobility of coating elements within the substrate. However, the RHEATF microstructure has exhibited large grains. The experimental evidence shows a microstructure slightly deviated from often reported characteristics of zone 1 thin solid films [57–59]. This may indicates that rapid grain nucleation and growth have occurred and a single-phase solid solution microstructure with well defined crystal structure was formed rather than an amorphous or complex multiphase material.

A proposed explanation on a possible accelerated kinetics of nucleation and growth in high-entropy alloy thin films (HEATF) have been recently investigated by Tunes *et al.* [48]. By means of comparing two thin films, a non-equiatomic and an equiatomic, the authors reported that in the latter case, the equiatomic condition has facilitated the growth of larger single-phase crystals (100–200 nm) while in the non-equiatomic film, the microstructure was of nanocrystalline nature with smaller grain-sizes (< 100 nm). This is due to the kinetics of nucleation of small embryos and their subsequent growth as studied by Hollomon and Turnbull [60] to be a process entirely governed by both volumetric Gibbs (ΔG_v) and surface energies (γ):

$$r^* = -\frac{2\gamma}{\Delta G_v} \quad (1)$$

Where r^* is known as critical radius for nucleation of an spherical-like dendrite embryo. Thus, in a defined high-entropy alloy metallic system, such as the NbTaMoW, the minimised Gibbs free

energy achieved by the equiatomic composition of the coating elements is a condition for promoting the nucleation of embryos with larger critical radii when compared with conventional terminal solid solution systems at non-equiatomic elemental compositions.

Analysis of results from the EFTEM carried out in the RHEATF prior annealing (figure 2) exhibiting that the material elements are uniformly distributed throughout the microstructure of the film in combination with the TEM analysis which has confirmed a single-phase BCC microstructure with large columnar is, therefore, an indicative that a high-entropy alloy has been formed at very low homologous temperature ($T/T_m=0.13$) where a typical zone 1 thin solid film is expected to have, according to Thornton [59], as a poorly defined microstructure. This suggests that the advent of the minimised Gibbs free energy is a key parameter which should be additionally incorporated within the theoretical conceptions of the structure-zone model proposed in 1969 by Movchan and Demchishin [58] and later modified by Thornton [57, 59], in order to accommodate possible accelerated mechanisms of nucleation and growth in these refractory and non-refractory high-entropy alloy thin films systems.

4.2. Ar bubbles and elemental segregation at the interface

One particular aspect in the microstructure of the deposited NbMoTaW RHEATF is the presence of voids or bubbles as revealed by the TEM characterisation. By means of defocusing the electron beam, voids and bubbles are responsive to phase contrast (or Fresnel contrast) which allowed their characterisation [61]. Conceptually, voids are considered an agglomerate of vacancies while a bubble can be viewed as cluster of both vacancies and inert gas atoms [61, 62]. For an equilibrium bubble, the internal pressure is a function of its measured radius and can be estimated as: $p = 2\gamma/r$. Due to the confirmation of Ar in the thin film, as showed in the EFTEM analysis in the figure 2, these small round particles are rather likely equilibrium bubbles than voids, however, their TEM contrast is believed to be very similar to the latter [61].

Voids and bubbles have already been reported previously to occur in sputter-deposited thin films. For instance, by means of analysing Au deposited thin films within a TEM, Lloyds *et al.* [63] observed a large number of voids that have nucleated in the matrix and at the grain boundaries of small Au crystallites. A detailed study on void formation in thin films has been conducted by Nakahara [64] who proposed that their formation is intimately associated with surface and volumetric migration of vacancies and incorporation of inert gas species into defective zones at the multi-atomic steps of the growing thin film. These authors also noted that microporosity due to voids and nucleation of bubbles is an inevitable and intrinsic phenomenon in the science of the thin films and the underlying mechanisms for its occurrence is not yet well understood [65]. At the same time from basic solid state physics principles one can expect creation of significant amounts of vacancies due to fast thermalisation of the arriving atomic species. These vacancies are expected to cluster, thus creating voids.

As mentioned previously, the microstructure sputter-deposited thin films at the zone 1 is associated with a typical columnar grain structure. Another microstructural property of a zone 1 microstructure is the growth of voided grain boundaries whose consist of defective regions where vacancies form and concentrate during deposition [59, 66–68] as depicted in the figure 8(a). A possible mechanism

to explain the nucleation of bubbles in the NbMoTaW RHEATF at such low deposition temperatures may involve implantation of Ar into the growing film as showed in the figure 8(b). Backscattering of Ar atoms from sputtering targets occur during sputtering and eventually, these Ar atoms have the necessary energy to reach the substrate and get implanted. As the solubility of inert gases is low in solids [61], the most energetic favourable sites for Ar atoms will be trapped within vacancies rather than dissolved in the random solid solution. The entrapment of Ar atoms is also enhanced due to ballistic collisions from the impinging coating elements that progressively reach the substrate [57, 59, 69]. At the trapped Ar specific site dependencies, bubbles will then grow upon the arrival of vacancies that are also mobile at the temperature range of deposition [70]. During the film growth, the voided open boundaries are also sources of vacancies for bubbles nucleation. As a consequence, Ar bubbles are observed in the matrix phase as showed in the figure 1(b).

After 10 hours of annealing at 523 K, Ar bubbles were also observed along the grain boundaries of the columnar grains as shown in figure 3(c). EFTEM of the thin film as-deposited (figure 2) showed that Ar accumulated at the interface of the film and the substrate, but after annealing, figure 4, the inert gas was not accumulated at the interface. Additionally, the EFTEM analysis for the annealed thin film has indicated that Ta, Mo and W accumulated at the interface between the film and the Si substrate while Nb remained within the thin film microstructure. From data in literature (table 2), self-diffusion of Nb is very low when compared with Mo, Ta and W. Mo is the fastest diffusive of all elements. This explains why Nb has not been observed at the interface. According to Wulf *et al.* it is well known that for zone 1 microstructures, the activation energies for migration of defects at the surface, grain boundaries and bulk are in the ratio of 1:2:4 [71]. Upon extended annealing time is likely that the grain boundary diffusion may cause a flux of vacancies and Ar towards these boundaries while coating elements, tend to migrate preferentially to the interface as depicted in figure 9. Due to the absence of phase transformations and/or precipitation in the microstructure, this elemental segregation was a marginal effect that have occurred at a relatively low temperatures, enhanced by the presence of voided grain boundaries and that was preferential for those coating elements with smaller atomic radii and higher self-diffusion coefficients (Mo, Ta and W).

A strong evidence to support the argument that grain boundary upon annealing played the dominant role rather than bulk diffusion in the RHEATF solid solution, can be noticed by means of estimating the sizes distribution of bubbles before and after annealing, as exhibited in the figure 5. One would expect a significant or even slightly growth of the bubbles size within the bulk. Such fact has not been observed to occur. In HEAs, the bulk mobility of lattice defects and solute atoms have been reported to be suppressed or mitigated [16, 20, 35]. The fact that bubbles have not grown also indicates neither coalescence nor vacancies incorporation have not significantly occurred.

As studied by Waterbeemd *et al.* [72], gaseous impurities such as O can have a substantial effect on the final microstructure of sputter-deposited thin solid films. Such active species reduce adatom mobilities, thus favouring the formation of zone 1 structures even at high-temperature deposition [73–75]. In this work, as confirmed by the EFTEM maps, O has been reliably detected only at the edge of the lamellae in the film as-deposited and in very low concentration after in-air annealing. O map after the annealing does not contain any meaningful quantitative information as its concentration is low for

the detection method used in this work.

Even that the microstructure has Ar bubbles – which are often reported to deteriorate a wide set of alloy properties [61] – the random solid solution remained stable under the conditions studied in this work: no phase transformation and no precipitation were observed after extended annealing.

4.3. High mechanical damage tolerance

The high hardness and Young's modulus combined with the high mechanical damage tolerance against nanoscratching allow the NbTaMoW RHEATF to be considered as a thin solid film with exceptional mechanical performance. Following the microstructural characterisation of the deposited thin film presented in this work, considerations on the origins of such interesting mechanical behavior can be made.

At a fundamental level, hardness is the capability of a material of resisting to plastic deformation. Nanoindentation measurements have indicated that the NbTaMoW RHEATF has a hardness around 22.8 ± 0.7 GPa before annealing and 16.0 ± 0.6 GPa after annealing which is comparable with most conventional ceramics. **As the annealing was performed in-air, the drop in the reduced modulus in the annealed film after a depth of 40 nm is associated to the formation of an oxide layer on the top of the RHEATF.** The origins of such high hardness are in the microstructure of the RHEATF at nanoscale. During deformation, the activation of dislocation sources in the RHEATF is clearly inhibited due to two main reasons: (i) confinement of grains at the nanocrystalline regime [76–78] and (ii) the chemical solid-solution disorder resulting in complex defect landscape and kinetics in high-entropy alloy systems which suppress the development of extended defects [16, 79, 80]. In addition to these facts, dislocation motion can also be affected by the presence of Ar bubbles. On the latter, inert gas bubbles are often perceived as associated with degradation of mechanical properties through embrittlement [61]. In the present set of the results, these bubbles were observed to not degrade the mechanical properties. This is particular evidenced by the nanoscratching results (figure 7) where the cracking of the RHEATF was not as catastrophic as in the case of the titanium nitride. Due to the microstructural features of the NbMoTaW RHEATF, the present results are suggesting that this thin solid film can simultaneously retain good crack resistance and high hardness level.

Both hardness and Young's modulus have dropped at around 30% after annealing. The electron microscopy characterisation of the RHEATF showed that Ar bubbles were also observed in the film microstructure after annealing, therefore the drop in the hardness is rather associated with relief of residual internal stresses [81, 82] than Ar bubble annihilation and thermal desorption of the Ar gas within the RHEATF. Additionally, after the extended annealing time, the Ar bubbles have not grown indicating that the high-entropy alloy core effects may be limiting the diffusion of point defects. In addition, it is worth to emphasise that the thin film was observed to be stable after extended annealing and neither significant grain growth and precipitation were observed.

5. Conclusions and further works

The synthesis of a refractory high-entropy alloy thin film of the system NbTaMoW is reported in this paper. Its microstructure is partially consistent with the Movchan-Demchishin-Thornton structure-zone models for zone 1 deposition parameters where low homologous temperatures ($T/T_m < 0.3$) does

not allow significant bulk diffusion and a columnar grain structure is observed. Unexpectedly, by means of EFTEM and conventional TEM characterisation, the thin films are of a well-defined random solid-solution with body-centred cubic structure as opposed to the previously reported common zone 1 thin film microstructures that often are reported to lack of a well defined crystal structure. High-entropy alloy, nucleation and growth theories were used to explain the microstructural features: at the equiatomic condition, larger critical radii for nucleation contributes for the rapid growth of the thin film embryos. This indicates that MDT structural-zone models are yet to be further modified for the class of thin films with minimised Gibbs free energies guaranteed by the equiatomic condition.

Ar bubbles have been observed throughout the microstructure of the thin film and a hypothesis of Ar implantation and entrapment due to ballistic processes has been proposed to explain their occurrence at low temperature, although the whole process is not yet well understood by thin film community [64, 73]. Ar bubbles grow upon the arrival of mobile vacancies during the stages of nucleation and growth of the random solid solution. The thin film after extended annealing have also exhibited Ar bubbles along grain boundaries and elemental segregation of Mo, Ta and W at the interface with the substrate. On the absence of phase transformations and/or precipitation in the microstructure of the annealed film, such segregation at the interfaces was attributed to the fast intergranular boundary diffusion of elements and vacancies, as bulk diffusion of solute atoms and lattice defects in high-entropy alloys have been recently reported to be suppressed and complex [35, 83]. This also agrees with the fact that matrix bubbles have not grown after annealing when compared with the thin film as-deposited.

Nanomechanical measurements indicated that the RHEATF is capable of retain – at the same time – high hardness (comparable with conventional ceramics) and an impressive damage tolerance against nanoscratching, thus indicating a high crack resistance. The origins of such high damage tolerance was attributed to its microstructural features at nanoscale in combination with well-known high-entropy alloy core effects.

Due to the observed phase stability of the RHEATF after extended moderate temperature in-air annealing, the high damage tolerance when compared with conventional ceramics and the nanocrystalline grain-sizes, these films can be considered potential candidates for applications in extreme environments, although further studies are needed to address the microstructure of RHEATFs at higher temperatures and its relationship with structure-zone models as well as the computer modelling of the impact on mechanical properties of inert gas bubbles formation during IBSD. The relationship between residual stresses, nucleation and growth kinetics and mechanical performance of these new RHEATFs are also yet to be addressed in future studies in order to investigate the role of the HEA core-effects in their properties especially when compared with conventional thin solid films.

6. Acknowledgements

The authors are grateful to the Engineering and Physical Sciences Research Council (EPSRC) for funding MIAMI facilities (grants number EP/E017266/1 and EP/M028283/1). MAT is grateful for Professor Stephen E. Donnelly (University of Huddersfield) and Dr. Philip D. Edmondson (Oak Ridge National Laboratory) to support his doctoral research. The authors thank Prof. Ben Beake

(Micro Materials Ltd) for cross-checking the nanomechanical results presented in this paper.

7. Data Availability

The raw and processed data required to reproduce these findings are available to download in the link doi:10.17632/3v9kj944d4.2 permanently stored at the Mendeley Data repository.

References

- [1] G. Routschka, *Refractory Materials: Pocket Manual; Design, Properties, Testing*, Vulkan-Verlag GmbH, 2008.
- [2] J. Wittenauer, Refractory metals 1990: old challenges, new opportunities, *JOM Journal of the Minerals, Metals and Materials Society* 42 (8) (1990) 7–7.
- [3] T. Moss, R. Davies, G. Barna, Refractory-alloy requirements for space power systems., Tech. rep., National Aeronautics and Space Administration, Cleveland, Ohio. Lewis Research Center (1970).
- [4] P. R. Subramanian, M. G. Mendiratta, D. M. Dimiduk, The development of Nb-based advanced intermetallic alloys for structural applications, *Jom* 48 (1) (1996) 33–38. doi:10.1007/BF03221360.
- [5] S. Zinkle, G. Was, Materials challenges in nuclear energy, *Acta Materialia* 61 (3) (2013) 735–758. doi:10.1016/j.actamat.2012.11.004.
URL <http://www.sciencedirect.com/science/article/pii/S1359645412007987>
- [6] P. Hosemann, J. Vujić, Material issues for current and advanced nuclear reactor designs, *Contemporary materials* 1 (5) (2014) 10–25. doi:10.7251/CM.V1I5.1493.
- [7] I. Cook, Materials research for fusion energy, *Nature Materials* 5 (2) (2006) 77–80. doi:10.1038/nmat1584.
URL <http://www.ncbi.nlm.nih.gov/pubmed/16449986><http://www.nature.com/doifinder/10.1038/nmat1584>
- [8] R. Gold, D. Harrod, Refractory metal alloys for fusion reactor applications, *Journal of Nuclear Materials* 85-86 (1979) 805–815. doi:10.1016/0022-3115(79)90359-3.
URL <https://www.sciencedirect.com/science/article/pii/0022311579903593>
- [9] Z. J. Zhang, M. M. Mao, J. Wang, B. Gludovatz, Z. Zhang, S. X. Mao, E. P. George, Q. Yu, R. O. Ritchie, Nanoscale origins of the damage tolerance of the high-entropy alloy CrMnFeCoNi, *Nature Communications* 6 (1) (2015) 10143. doi:10.1038/ncomms10143.
- [10] C.-H. Chang, M. S. Titus, J.-W. Yeh, Oxidation behavior between 700 and 1300c of refractory tizrnbhfta high-entropy alloys containing aluminum, *Advanced Engineering Materials* (2018) 1700948.
- [11] X. Fu, C. Schuh, E. Olivetti, Materials selection considerations for high entropy alloys, *Scripta Materialia* 138 (2017) 145–150.
- [12] Y. Ye, Q. Wang, J. Lu, C. Liu, Y. Yang, High-entropy alloy: challenges and prospects, *Materials Today* 19 (6) (2016) 349–362. doi:10.1016/j.mattod.2015.11.026.
- [13] J. W. Yeh, Y. L. Chen, S. J. Lin, S. K. Chen, High-entropy alloys—a new era of exploitation, in: *Materials Science Forum*, Vol. 560, Trans Tech Publ, 2007, pp. 1–9.
- [14] A. Gali, E. George, Tensile properties of high- and medium-entropy alloys, *Intermetallics* 39 (2013) 74–78. doi: <https://doi.org/10.1016/j.intermet.2013.03.018>.
URL <http://www.sciencedirect.com/science/article/pii/S0966979513000903>
- [15] B. S. Murty, J.-W. J. Yeh, S. Ranganathan, *High-Entropy Alloys*, Butterworth-Heinemann, 2014. doi:10.1016/B978-0-12-800251-3.00002-X.
URL <http://linkinghub.elsevier.com/retrieve/pii/B978012800251300002X>
- [16] Y. Zhang, G. M. Stocks, K. Jin, C. Lu, H. Bei, B. C. Sales, L. Wang, L. K. Béland, R. E. Stoller, G. D. Samolyuk, M. Caro, A. Caro, W. J. Weber, Influence of chemical disorder on energy dissipation and defect evolution in concentrated solid solution alloys, *Nature Communications* 6 (2015) 8736. arXiv:9809069v1, doi:10.1038/ncomms9736.
URL <http://www.nature.com/doifinder/10.1038/ncomms9736>
- [17] J.-W. Yeh, S.-K. Chen, S.-J. Lin, J.-Y. Gan, T.-S. Chin, T.-T. Shun, C.-H. Tsau, S.-Y. Chang, Nanostructured High-Entropy Alloys with Multiple Principal Elements: Novel Alloy Design Concepts and Outcomes, *Advanced Engineering Materials* 6 (5) (2004) 299–303. doi:10.1002/adem.200300567.
URL <http://doi.wiley.com/10.1002/adem.200300567>
- [18] B. Cantor, I. Chang, P. Knight, A. Vincent, Microstructural development in equiatomic multicomponent alloys, *Materials Science and Engineering: A* 375-377 (2004) 213–218. doi:10.1016/j.msea.2003.10.257.
URL <http://www.sciencedirect.com/science/article/pii/S0921509303009936>

- [19] S. Ranganathan, *Alloyed pleasures: Multimetallurgical cocktails*, Indian Academy of Sciences, 2003.
URL http://eprints.iisc.ernet.in/6189/1/Alloyed_{_}pleasures.pdf
- [20] F. Granberg, K. Nordlund, M. W. Ullah, K. Jin, C. Lu, H. Bei, L. M. Wang, F. Djurabekova, W. J. Weber, Y. Zhang, Mechanism of radiation damage reduction in equiatomic multicomponent single phase alloys, *Phys. Rev. Lett.* 116 (April) (2016) 135504. doi:10.1103/PhysRevLett.116.135504.
- [21] B. Kombariah, K. Jin, H. Bei, P. Edmondson, Y. Zhang, Phase stability of single phase $\text{Al}_{0.12}\text{CrNiFeCo}$ high entropy alloy upon irradiation, *Materials & Design* 160 (2018) 1208–1216.
- [22] O. N. Senkov, G. B. Wilks, D. B. Miracle, C. P. Chuang, P. K. Liaw, Refractory high-entropy alloys, *Intermetallics* 18 (9) (2010) 1758–1765. doi:10.1016/j.intermet.2010.05.014.
URL <https://www.sciencedirect.com/science/article/pii/S0966979510002475>
- [23] S. Praveen, H. S. Kim, High-entropy alloys potential candidates for high-temperature applications an overview, *Advanced Engineering Materials* 20 (1) (2018) 1700645. doi:10.1002/adem.201700645.
- [24] O. N. Senkov, D. B. Miracle, K. J. Chaput, J.-P. Couzinie, Development and exploration of refractory high entropy alloys—a review, *Journal of Materials Research* (2018) 1–37.
- [25] C.-M. Lin, C.-C. Juan, C.-H. Chang, C.-W. Tsai, J.-W. Yeh, Effect of Al addition on mechanical properties and microstructure of refractory $\text{Al}_{0.12}\text{CrNiFeCo}$ alloys, *Journal of Alloys and Compounds* 624 (2015) 100–107.
- [26] F. G. Coury, T. Butler, K. Chaput, A. Saville, J. Copley, J. Foltz, P. Mason, K. Clarke, M. Kaufman, A. Clarke, Phase equilibria, mechanical properties and design of quaternary refractory high entropy alloys, *Materials & Design*.
- [27] L.-Y. Tian, G. Wang, J. S. Harris, D. L. Irving, J. Zhao, L. Vitos, Alloying effect on the elastic properties of refractory high-entropy alloys, *Materials & Design* 114 (2017) 243–252.
- [28] Y. Zhang, T. T. Zuo, Z. Tang, M. C. Gao, K. A. Dahmen, P. K. Liaw, Z. P. Lu, Microstructures and properties of high-entropy alloys, *Progress in Materials Science* 61 (2014) 1–93.
- [29] X. Wang, Y. Zhang, Y. Qiao, G. Chen, Novel microstructure and properties of multicomponent CoCrCuFeNiTi alloys, *Intermetallics* 15 (3) (2007) 357–362.
- [30] Y. Zhang, X. Yang, P. Liaw, Alloy design and properties optimization of high-entropy alloys, *Jom* 64 (7) (2012) 830–838.
- [31] B. Gludovatz, A. Hohenwarter, D. Catoor, E. H. Chang, E. P. George, R. O. Ritchie, A fracture-resistant high-entropy alloy for cryogenic applications, *Science* 345 (6201) (2014) 1153–1158.
- [32] O. Senkov, J. Scott, S. Senkova, D. Miracle, C. Woodward, Microstructure and room temperature properties of a high-entropy $\text{Ta}_{0.1}\text{Nb}_{0.1}\text{Zr}_{0.1}\text{Ti}_{0.1}\text{Hf}_{0.1}\text{V}_{0.1}\text{W}_{0.1}$ alloy, *Journal of alloys and compounds* 509 (20) (2011) 6043–6048.
- [33] C. G. Schoen, T. Duong, Y. Wang, R. Arroyave, A proof of concept: Thermodynamics of aluminum – transition metal highly concentrated alloys, *Journal of Alloys and Compounds* 781 (2019) 595 – 605. doi:<https://doi.org/10.1016/j.jallcom.2018.12.068>.
URL <http://www.sciencedirect.com/science/article/pii/S0925838818346152>
- [34] O. Senkov, G. Wilks, J. Scott, D. Miracle, Mechanical properties of $\text{Nb}_{25}\text{Mo}_{25}\text{Ta}_{25}\text{W}_{25}$ and $\text{V}_{20}\text{Nb}_{20}\text{Mo}_{20}\text{Ta}_{20}\text{W}_{20}$ refractory high entropy alloys, *Intermetallics* 19 (5) (2011) 698–706. doi:10.1016/J.INTERMET.2011.01.004.
URL <https://www.sciencedirect.com/science/article/pii/S0966979511000185>
- [35] C. Liu, H. Wang, S. Zhang, H. Tang, A. Zhang, Microstructure and oxidation behavior of new refractory high entropy alloys, *Journal of Alloys and Compounds* 583 (2014) 162–169. doi:10.1016/j.jallcom.2013.08.102.
URL <https://www.sciencedirect.com/science/article/pii/S0925838813019634>
- [36] O. Senkov, S. Senkova, C. Woodward, Effect of aluminum on the microstructure and properties of two refractory high-entropy alloys, *Acta Materialia* 68 (2014) 214–228. doi:10.1016/J.ACTAMAT.2014.01.029.
URL <https://www.sciencedirect.com/science/article/pii/S1359645414000469>
- [37] Y. Wu, Y. Cai, X. Chen, T. Wang, J. Si, L. Wang, Y. Wang, X. Hui, Phase composition and solid solution strengthening effect in $\text{Ti}_{0.1}\text{Zr}_{0.1}\text{Nb}_{0.1}\text{Mo}_{0.1}\text{V}_{0.1}\text{W}_{0.1}$ high-entropy alloys, *Materials & Design* 83 (2015) 651–660.
- [38] C. C. Juan, M. H. Tsai, C. W. Tsai, C. M. Lin, W. R. Wang, C. C. Yang, S. K. Chen, S. J. Lin, J. W. Yeh, Enhanced mechanical properties of HfMoTaTiZr and HfMoNbTaTiZr refractory high-entropy alloys, *Intermetallics* 62 (2015) 76–83. doi:10.1016/j.intermet.2015.03.013.
URL <https://www.sciencedirect.com/science/article/pii/S0966979515000643>
- [39] B. Gorr, M. Azim, H. J. Christ, T. Mueller, D. Schliephake, M. Heilmaier, Phase equilibria, microstructure, and high temperature oxidation resistance of novel refractory high-entropy alloys, *Journal of Alloys and Compounds* 624 (2015) 270–278. doi:10.1016/j.jallcom.2014.11.012.
URL <https://www.sciencedirect.com/science/article/pii/S0925838814026553>
- [40] M. S. Anzorena, A. Bertolo, L. Galletti, A. Kreiner, H. Mosca, G. Bozzolo, M. del Grosso, Characterization and modeling of a $\text{Mo}_{0.1}\text{V}_{0.1}\text{W}_{0.1}\text{Zr}_{0.1}\text{Ti}_{0.1}\text{Hf}_{0.1}$ high entropy alloy, *Materials & Design* 111 (2016) 382–388.
- [41] Y. Zou, S. Maiti, W. Steurer, R. Spolenak, Size-dependent plasticity in an $\text{Nb}_{25}\text{Mo}_{25}\text{Ta}_{25}\text{W}_{25}$ refractory high-entropy alloy, *Acta Materialia* 65 (2014) 85–97. doi:10.1016/j.actamat.2013.11.049.
URL <https://www.sciencedirect.com/science/article/pii/S1359645413009075>
<http://linkinghub.elsevier.com/retrieve/pii/S1359645413009075>

- [42] B. Braeckman, F. Boydens, H. Hidalgo, P. Dutheil, M. Jullien, A.-L. Thomann, D. Depla, High entropy alloy thin films deposited by magnetron sputtering of powder targets, *Thin Solid Films* 580 (2015) 71–76.
- [43] A. Marshal, K. G. Pradeep, D. Music, S. Zaefferer, P. De, J. M. Schneider, Combinatorial synthesis of high entropy alloys: Introduction of a novel, single phase, body-centered-cubic fcc solid solution, *Journal of Alloys and Compounds* 691 (2017) 683–689.
- [44] P. Malinovskis, S. Fritze, L. Riekehr, L. von Fieandt, J. Cedervall, D. Rehnlund, L. Nyholm, E. Lewin, U. Jansson, Synthesis and characterization of multicomponent (crnbctatiw) c films for increased hardness and corrosion resistance, *Materials & Design* 149 (2018) 51–62.
- [45] S.-C. Liang, Z.-C. Chang, D.-C. Tsai, Y.-C. Lin, H.-S. Sung, M.-J. Deng, F.-S. Shieu, Effects of substrate temperature on the structure and mechanical properties of (tivrzhf) n coatings, *Applied Surface Science* 257 (17) (2011) 7709–7713.
- [46] X. Feng, J. Zhang, Z. Xia, W. Fu, K. Wu, G. Liu, J. Sun, Stable nanocrystalline nbmotaw high entropy alloy thin films with excellent mechanical and electrical properties, *Materials Letters* 210 (2018) 84–87.
- [47] A. Andreev, L. Shaginyan, S. Firstov, M. Karpets, Danilenko, High-entropy coatings—structure and properties, *Journal of Superhard Materials* 40 (2) (2018) 88–101.
- [48] M. A. Tunes, V. M. Vishnyakov, S. E. Donnelly, Synthesis and characterisation of high-entropy alloy thin films as candidates for coating nuclear fuel cladding alloys, *Thin Solid Films* 649 (2018) 115 – 120. doi:<https://doi.org/10.1016/j.tsf.2018.01.041>.
URL <http://www.sciencedirect.com/science/article/pii/S0040609018300579>
- [49] C. A. Schuh, Nanoindentation studies of materials, *Materials today* 9 (5) (2006) 32–40.
- [50] J. Colligon, V. Vishnyakov, R. Valizadeh, S. E. Donnelly, S. Kumashiro, Study of nanocrystalline tin/si₃n₄ thin films deposited using a dual ion beam method, *Thin Solid Films* 485 (1-2) (2005) 148–154.
- [51] J. Trincavelli, S. Limandri, R. Bonetto, Standardless quantification methods in electron probe microanalysis, *Spectrochimica Acta Part B: Atomic Spectroscopy* 101 (2014) 76 – 85. doi:<https://doi.org/10.1016/j.sab.2014.07.016>.
URL <http://www.sciencedirect.com/science/article/pii/S0584854714001566>
- [52] L. Giannuzzi, F. Stevie, A review of focused ion beam milling techniques for TEM specimen preparation, *Micron* 30 (3) (1999) 197–204. doi:10.1016/S0968-4328(99)00005-0.
URL <http://www.sciencedirect.com/science/article/pii/S0968432899000050>
- [53] C. A. Schneider, W. S. Rasband, K. W. Eliceiri, Nih image to imagej: 25 years of image analysis, *Nature methods* 9 (7) (2012) 671.
- [54] B. Beake, V. Vishnyakov, A. Harris, Nano-scratch testing of (ti, fe) nx thin films on silicon, *Surface and Coatings Technology* 309 (2017) 671–679.
- [55] B. Fultz, J. M. Howe, *Transmission electron microscopy and diffractometry of materials*, Springer Science & Business Media, 2012.
- [56] M. Hellenbrandt, The inorganic crystal structure database (icsd)—present and future, *Crystallography Reviews* 10 (1) (2004) 17–22.
- [57] J. A. Thornton, Influence of apparatus geometry and deposition conditions on the structure and topography of thick sputtered coatings, *Journal of Vacuum Science and Technology* 11 (4) (1974) 666–670.
- [58] B. Movchan, A. Demchishin, Structure and properties of thick condensates of nickel, titanium, tungsten, aluminium oxides, and zirconium oxides in vacuum., *Fiz. Metal. Metalloved.* 28: 653-60 (Oct 1969).
- [59] J. A. Thornton, High Rate Thick Film Growth, *Annual Review of Materials Science* 7 (1) (1977) 239–260. doi:10.1146/annurev.ms.07.080177.001323.
URL <http://www.annualreviews.org/doi/10.1146/annurev.ms.07.080177.001323>
- [60] J. H. Hollomon, D. Turnbull, Nucleation, *Progress in Metal Physics* 4 (1953) 333–388. doi:10.1016/0502-8205(53)90020-3.
- [61] S. Donnelly, The density and pressure of helium in bubbles in implanted metals: a critical review, *Radiation Effects* 90 (1-2) (1985) 1–47.
- [62] R. Rau, R. Ladd, J. Moteff, Voids in irradiated tungsten and molybdenum, *Journal of Nuclear Materials* 33 (3) (1969) 324–327. doi:10.1016/0022-3115(69)90029-4.
URL <http://www.sciencedirect.com/science/article/pii/0022311569900294>
- [63] J. Lloyd, S. Nakahara, Voids in thin as-deposited gold films prepared by vapor deposition, *Journal of Vacuum Science and Technology* 14 (1) (1977) 655–659.
- [64] S. Nakahara, Microporosity induced by nucleation and growth processes in crystalline and non-crystalline films, *Thin Solid Films* 45 (3) (1977) 421–432. doi:10.1016/0040-6090(77)90229-2.
- [65] P. M. Fabis, Microporosity in 304 stainless steel films prepared by vapor quenching, *Thin solid films* 128 (1-2) (1985) 57–66.
- [66] A. Dirks, H. Leamy, Columnar microstructure in vapor-deposited thin films, *Thin Solid Films* 47 (3) (1977) 219–233.
- [67] H. Fritzsche, M. Tanielian, C. C. Tsai, P. J. Gaczi, Hydrogen content and density of plasma-deposited amorphous

- silicon-hydrogen, *Journal of Applied Physics* 50 (5) (1979) 3366–3369.
- [68] S. Kim, J. Henderson, P. Chaudhari, Computer simulation of amorphous thin films of hard spheres, *Thin Solid Films* 47 (2) (1977) 155–158.
- [69] H. F. Winters, E. Kay, Gas incorporation into sputtered films, *Journal of Applied Physics* 38 (10) (1967) 3928–3934. doi:10.1063/1.1709043.
- [70] P. Ehrhart, P. Jung, H. Schultz, *Atomare Fehlstellen in Metallen*, Vol. 25, Springer, 1991.
- [71] J. Wulff, W. Moffatt, G. Pearsall, J. Brophy, R. Rose, H. Hayden, L. Shepard, J. Klerer, The structure and properties of materials, *Journal of The Electrochemical Society* 114 (9) (1967) 243C–250C.
- [72] J. Van de Waterbeemd, G. Van Oosterhout, Effect of the mobility of metal atoms on the structure of thin films deposited at oblique incidence, *Philips Res. Rep* 22 (1967) 375–387.
- [73] J. A. Thornton, The microstructure of sputter-deposited coatings, *Journal of Vacuum Science & Technology A: Vacuum, Surfaces, and Films* 4 (6) (1986) 3059–3065. doi:10.1116/1.573628.
URL <http://avs.scitation.org/doi/10.1116/1.573628>
- [74] H. Leamy, A. Dirks, Microstructure and magnetism in amorphous rare-earth-transition-metal thin films. i. microstructure, *Journal of Applied Physics* 49 (6) (1978) 3430–3438.
- [75] J. Venables, G. Price, GL Price in *Epitaxial Growth*, JW Matthews, ed, Vol. B, Academic Press, NY, 1975.
- [76] A. Hasnaoui, H. Van Swygenhoven, P. Derlet, Dimples on nanocrystalline fracture surfaces as evidence for shear plane formation, *Science* 300 (5625) (2003) 1550–1552.
- [77] A. R. Kalidindi, C. A. Schuh, Stability criteria for nanocrystalline alloys, *Acta Materialia* 132 (2017) 128–137.
- [78] A. J. Detor, C. A. Schuh, Tailoring and patterning the grain size of nanocrystalline alloys, *Acta Materialia* 55 (1) (2007) 371–379.
- [79] Y. Zhang, S. Zhao, W. J. Weber, K. Nordlund, F. Granberg, F. Djurabekova, Atomic-level heterogeneity and defect dynamics in concentrated solid-solution alloys, *Current Opinion in Solid State and Materials Science* 21 (5) (2017) 221–237.
- [80] Y. N. Osetsky, L. K. Beland, A. V. Barashev, Y. Zhang, On the existence and origin of sluggish diffusion in chemically disordered concentrated alloys, *Current Opinion in Solid State and Materials Science* 22 (3) (2018) 65 – 74. doi:<https://doi.org/10.1016/j.cossms.2018.05.003>.
URL <http://www.sciencedirect.com/science/article/pii/S135902861830038X>
- [81] A. Korsunsky, E. Salvati, A. Lunt, T. Sui, M. Mughal, R. Daniel, J. Keckes, E. Bemporad, M. Sebastiani, Nanoscale residual stress depth profiling by focused ion beam milling and eigenstrain analysis, *Materials & Design* 145 (2018) 55–64.
- [82] A. Engwall, Z. Rao, E. Chason, Origins of residual stress in thin films: Interaction between microstructure and growth kinetics, *Materials & Design* 110 (2016) 616–623.
- [83] C. G. Schön, T. Duong, Y. Wang, R. Arróyave, Probing the entropy hypothesis in highly concentrated alloys, *Acta Materialia* 148 (2018) 263–279. doi:10.1016/j.actamat.2018.01.028.
- [84] W. Gordy, W. O. Thomas, Electronegativities of the elements, *The Journal of Chemical Physics* 24 (2) (1956) 439–444.
- [85] J. R. Davis, *Metals handbook*, ASM international, 1998.
- [86] J. N. Mundy, S. J. Rothman, N. Q. Lam, H. A. Hoff, L. J. Nowicki, Self-diffusion in tungsten, *Physical Review B* 18 (12) (1978) 6566–6575. arXiv:arXiv:1011.1669v3, doi:10.1103/PhysRevB.18.6566.
- [87] F. Hutchinson, The Self-Diffusion Coefficient of Argon, *Physical Review* 72 (12) (1947) 1256. doi:10.1103/PhysRev.72.1256.
- [88] R. Einziger, J. Mundy, H. Hoff, Niobium self-diffusion, *Physical Review B* 17 (2) (1978) 440.
- [89] R. Pawel, T. Lundy, The diffusion of nb95 and ta182 in tantalum, *Journal of Physics and Chemistry of Solids* 26 (6) (1965) 937–942.

Contents

1	Introduction	2
2	Materials and methods	3
3	Results	4
4	Discussion	6
4.1	Relationships between sputter-deposition and the microstructures	6
4.2	Ar bubbles and elemental segregation at the interface	7
4.3	High mechanical damage tolerance	9
5	Conclusions and further works	9
6	Acknowledgements	10
7	Data Availability	11

List of Figures

1	The microstructure of the NbTaMoW RHEATF before annealing showing the BFTEM micrographs (a) and (d) at focus, and (b) underfocused (300 nm of defocus degree). The micrographs (c), (e) and (f) are DFTEM with the selected reflections indicated in the DP insets within micrographs (b) and (d). Note: SAED aperture covers all the field view in images (a) and (d); the scale bar in (a) also applies to (b-c) and the scale marker in (d) also applies to (e-f).	17
2	EFTEM elemental maps for the NbTaMoW RHEATF before annealing.	18
3	The microstructure of the NbTaMoW RHEATF after annealing showing: (a) BFTEM at focus, (b) BFTEM underfocused (300 nm of defocus degree) and (c) DFTEM. Note: The inset in (a) represents the diffraction pattern of the selected area and the SAED aperture covers all the field view in the image (a); the scale bar in (a) also applies to (b-c).	19
4	EFTEM elemental maps for the NbTaMoW RHEATF after annealing at 523 K during 10 hours.	20
5	Bubbles sizes distributions before and after extended in-air annealing at 523 K. . . .	21
6	Nanoindentation analysis for the RHEATF as-deposited and after annealing showing: (a) the hardness and (b) the reduced Young's modulus.	22
7	SEM micrographs of the nanoscratching traces for ramped load in the (a) NbMoTaW RHEATF and (b) TiN. Note: measurements were taken with the thin films as-deposited and the scale bar in (b) also applies to (a).	23
8	(a) The growth of a columnar grain structure in the stage 1 is accelerated by larger critical radius for embryo nucleation as Gibbs free energy is minimised by the HEA theory. (b) During the deposition, Ar backscattered atoms can reach the substrate and bubbles form due to collisions (i) and direct implantation (ii) processes at low deposition temperatures.	24
9	In a stage 1 columnar structure during annealing, vacancies and coating elements have preferential directions for migration. Grain boundary diffusion is faster than bulk [59, 71].	25

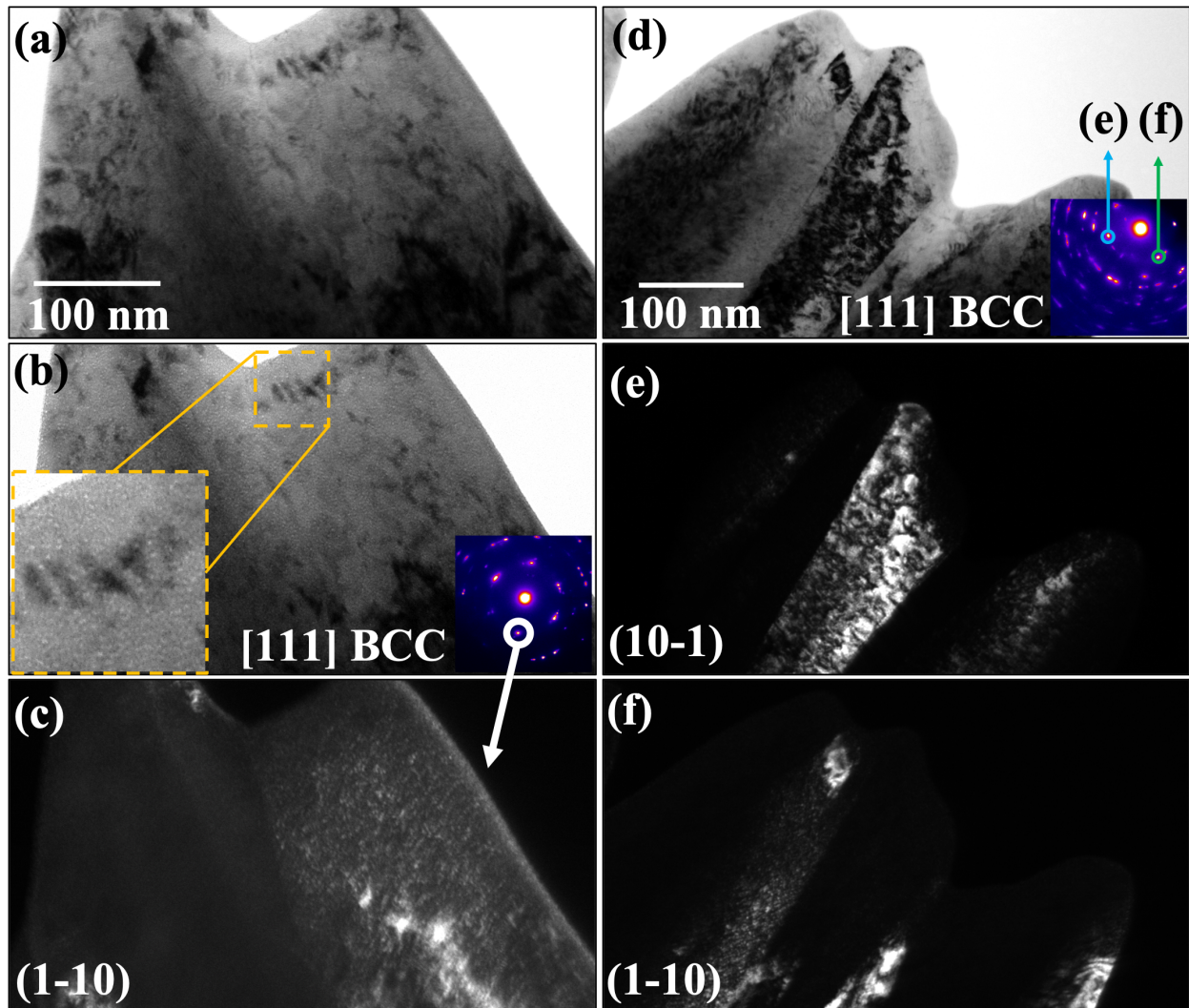


Figure 1: The microstructure of the NbTaMoW RHEATF before annealing showing the BFTEM micrographs (a) and (d) at focus, and (b) underfocused (300 nm of defocus degree). The micrographs (c), (e) and (f) are DFTEM with the selected reflections indicated in the DP insets within micrographs (b) and (d). Note: SAED aperture covers all the field view in images (a) and (d); the scale bar in (a) also applies to (b-c) and the scale marker in (d) also applies to (e-f).

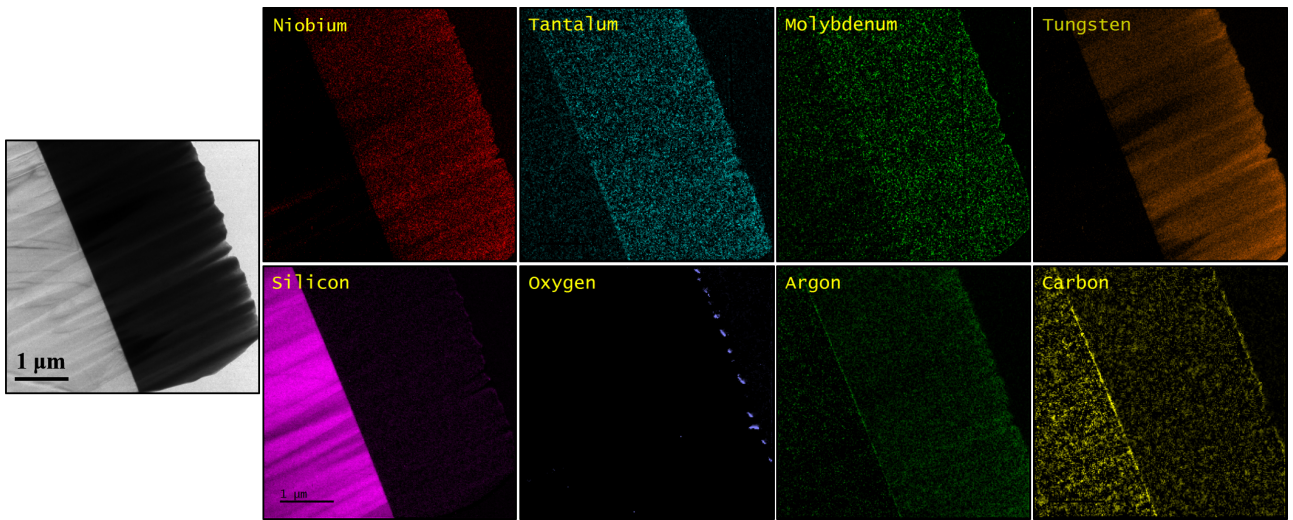


Figure 2: EFTEM elemental maps for the NbTaMoW RHEATF before annealing.

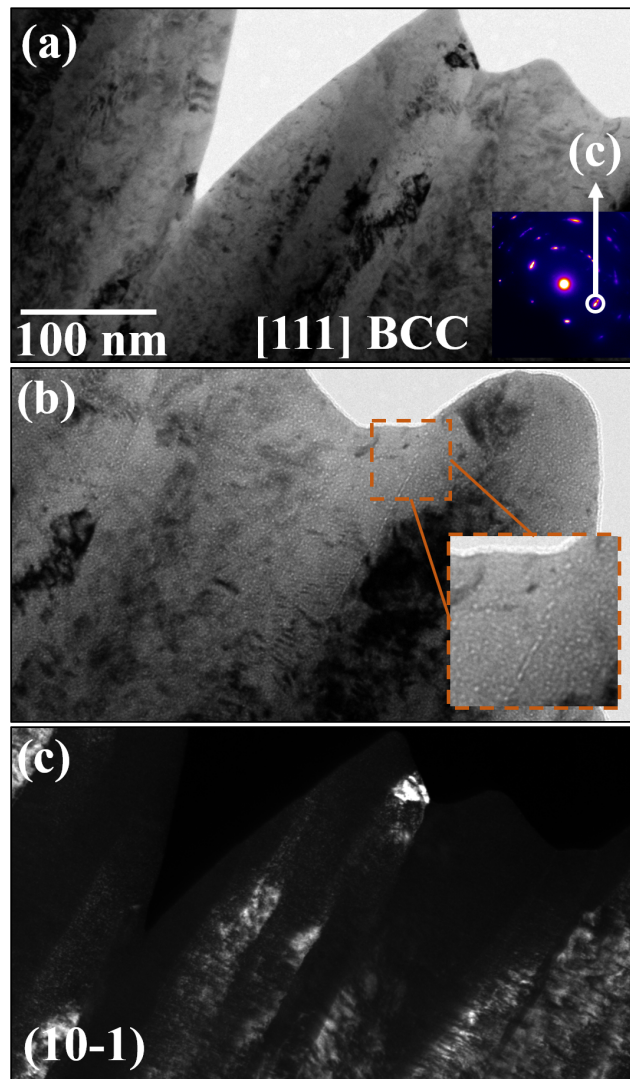


Figure 3: The microstructure of the NbTaMoW RHEATF after annealing showing: (a) BFTEM at focus, (b) BFTEM underfocused (300 nm of defocus degree) and (c) DFTEM. Note: The inset in (a) represents the diffraction pattern of the selected area and the SAED aperture covers all the field view in the image (a); the scale bar in (a) also applies to (b-c).

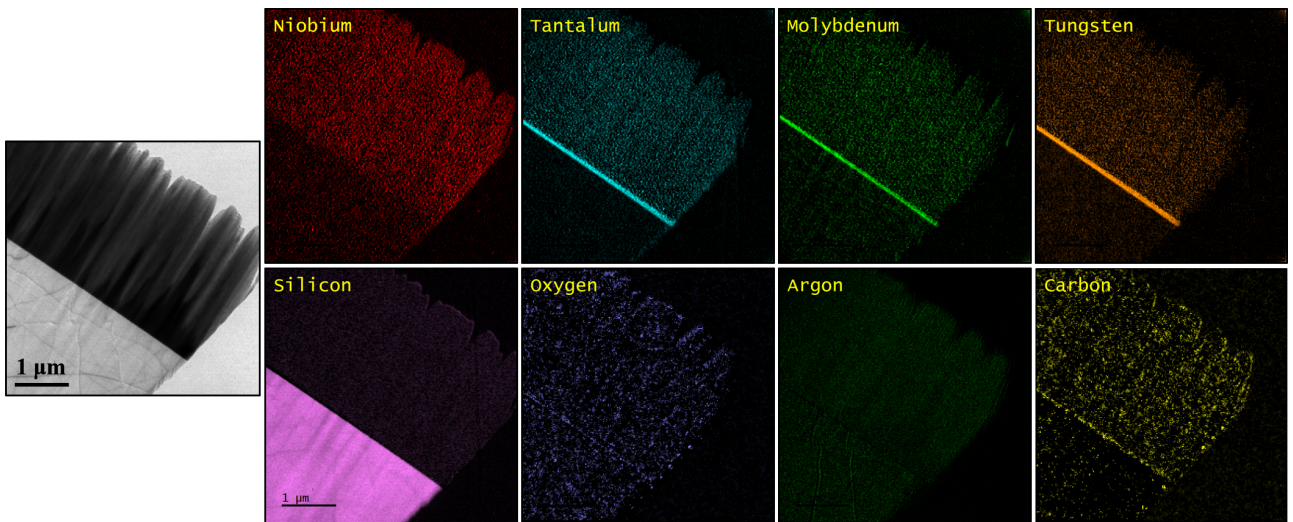


Figure 4: EFTEM elemental maps for the NbTaMoW RHEATF after annealing at 523 K during 10 hours.

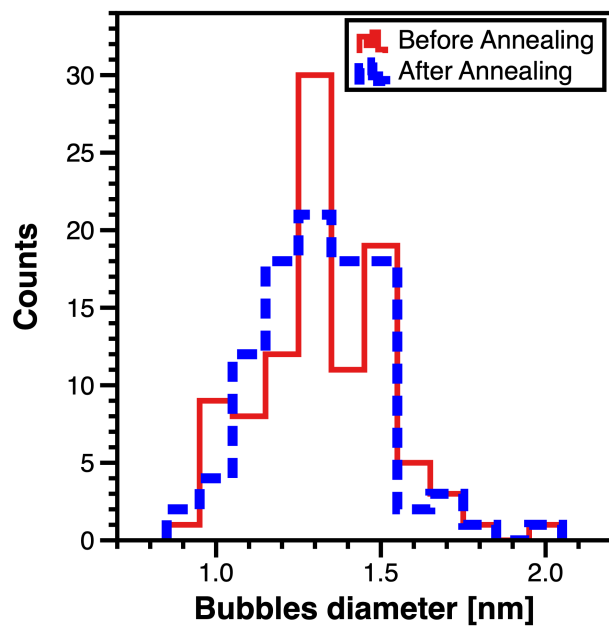


Figure 5: Bubbles sizes distributions before and after extended in-air annealing at 523 K.

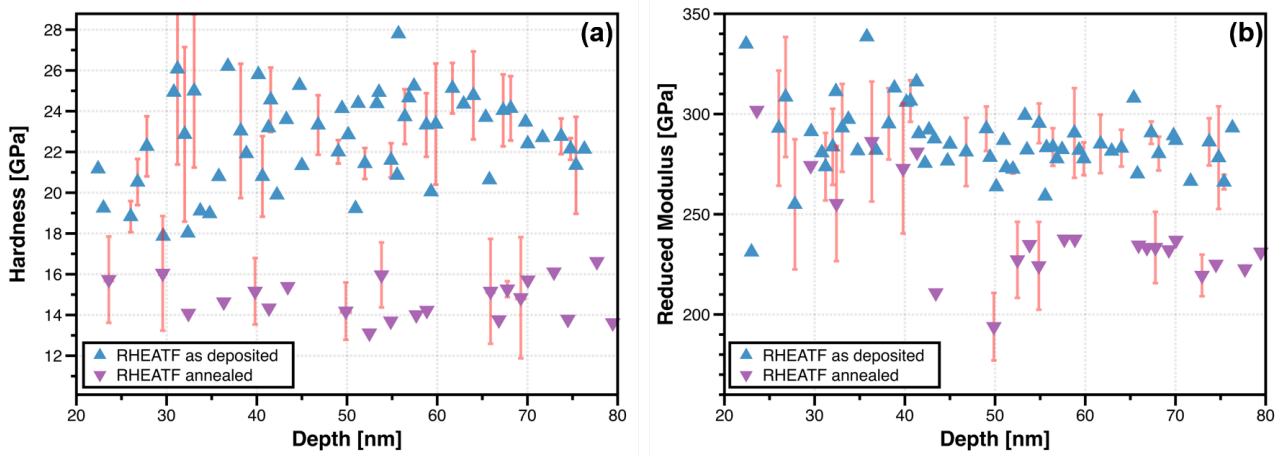


Figure 6: Nanoindentation analysis for the RHEATF as-deposited and after annealing showing: (a) the hardness and (b) the reduced Young's modulus.

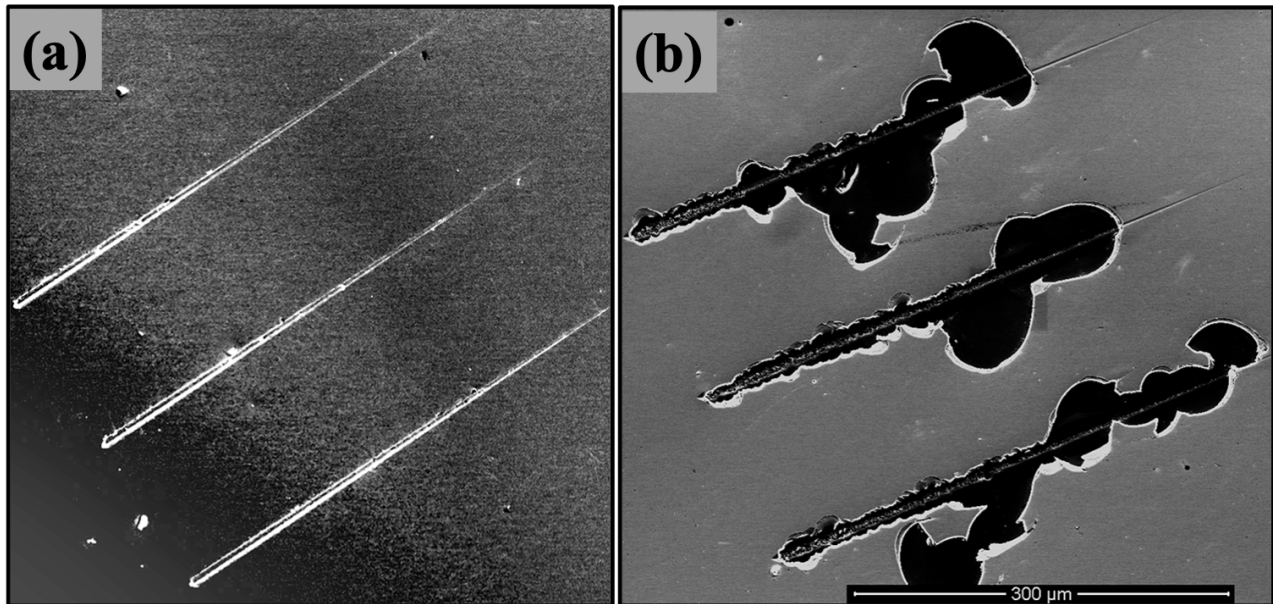


Figure 7: SEM micrographs of the nanoscratching traces for ramped load in the (a) NbMoTaW RHEATF and (b) TiN. Note: measurements were taken with the thin films as-deposited and the scale bar in (b) also applies to (a).

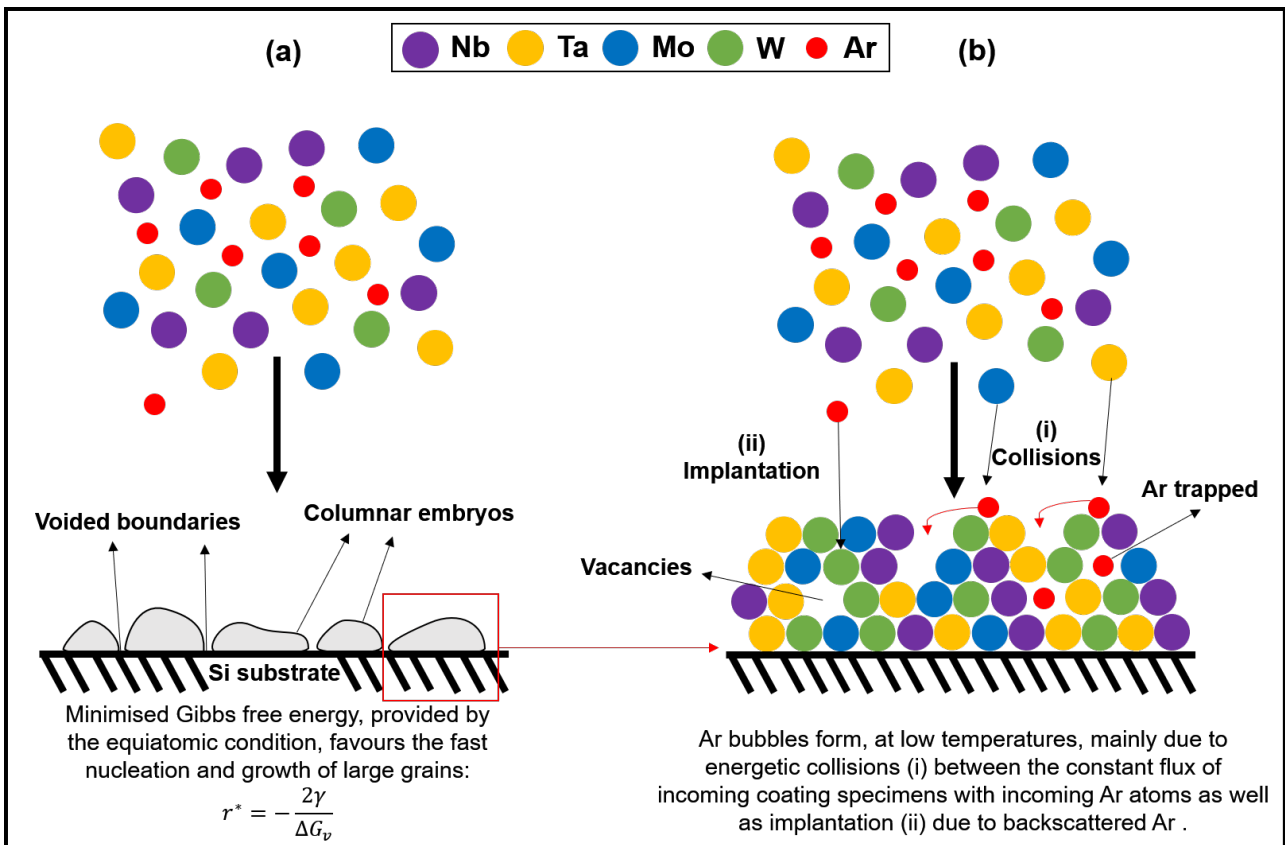


Figure 8: (a) The growth of a columnar grain structure in the stage 1 is accelerated by larger critical radius for embryo nucleation as Gibbs free energy is minimised by the HEA theory. (b) During the deposition, Ar backscattered atoms can reach the substrate and bubbles form due to collisions (i) and direct implantation (ii) processes at low deposition temperatures.

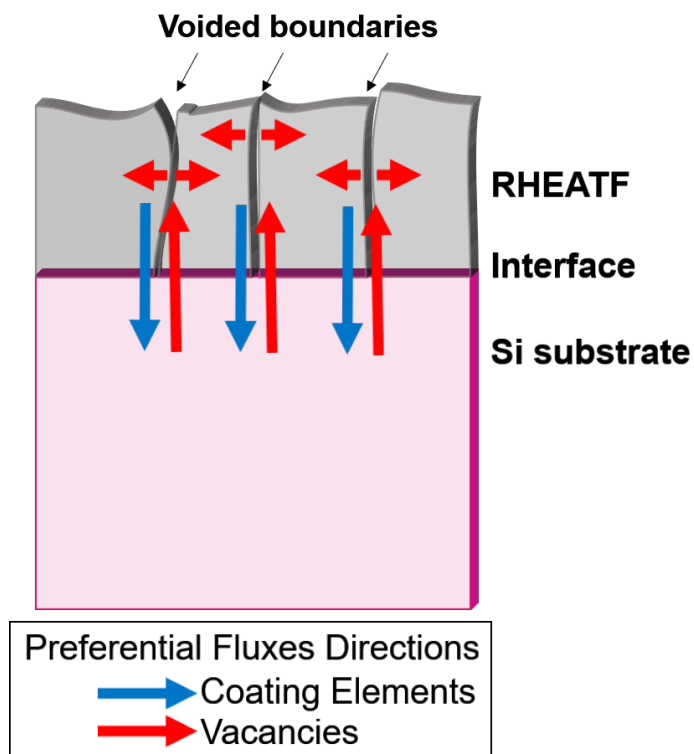


Figure 9: In a stage 1 columnar structure during annealing, vacancies and coating elements have preferential directions for migration. Grain boundary diffusion is faster than bulk [59, 71].

List of Tables

1 Elemental Composition of the ion beam sputter-deposited NbTaMoW RHEATF. . . . 27
2 Compiled list of BCC refractory metals properties. 28

Table 1: Elemental Composition of the ion beam sputter-deposited NbTaMoW RHEATF.

Elements	Atomic Percent [at.%]
Nb	23.2 ± 1.2
Mo	29.3 ± 1.5
Ta	23.1 ± 1.2
W	24.4 ± 1.2

Table 2: Compiled list of BCC refractory metals properties.

	Nb	Mo	Ta	W	Ref.
Electronegativity [eV]	1.60	2.16	1.50	2.36	[84]
Atomic radius [Å]	1.82	1.72	1.71	1.65	[85]
Max. Diff. Coef.† [cm ² ·s ⁻¹]	8.0×10 ⁻³	1.0×10 ⁻¹	1.8×10 ⁻²	4.0×10 ⁻²	[86–89]
Melting point [K]	2750	2896	3695	3290	[85]
Density [g·cm ⁻³]	8.6	10.3	16.7	19.3	[22]

† Maximum diffusion coefficient (at an infinite temperature). Representing diffusion by single vacancies [86].

Figure 1
[Click here to download high resolution image](#)

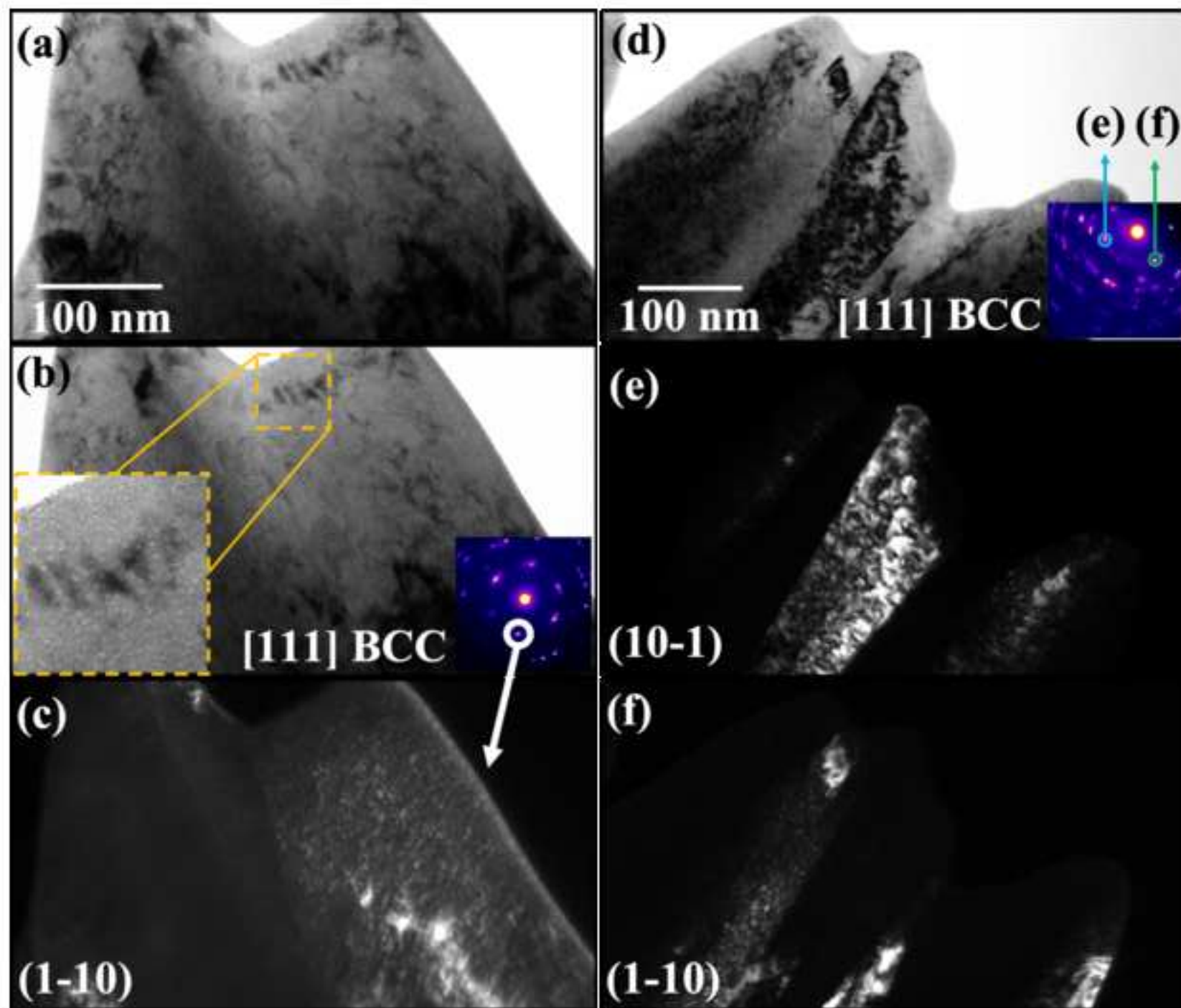


Figure 2
[Click here to download high resolution image](#)

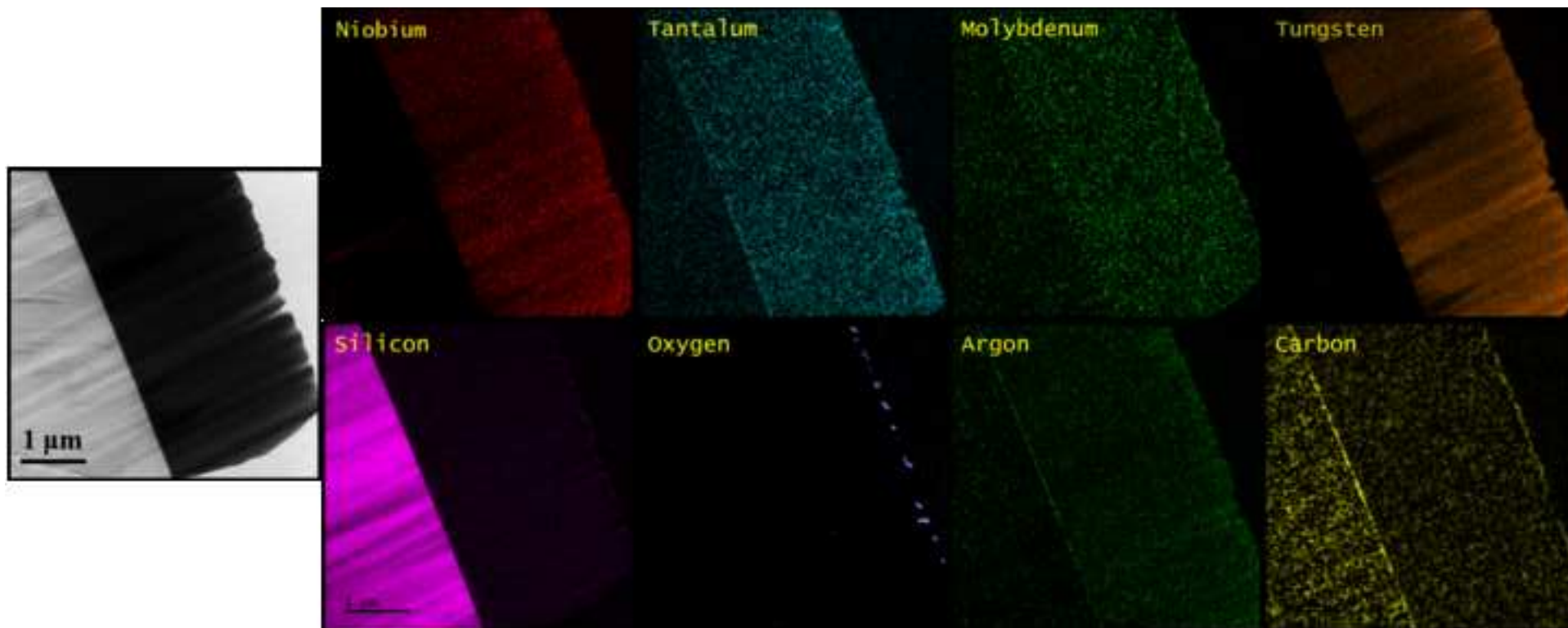


Figure 3
[Click here to download high resolution image](#)

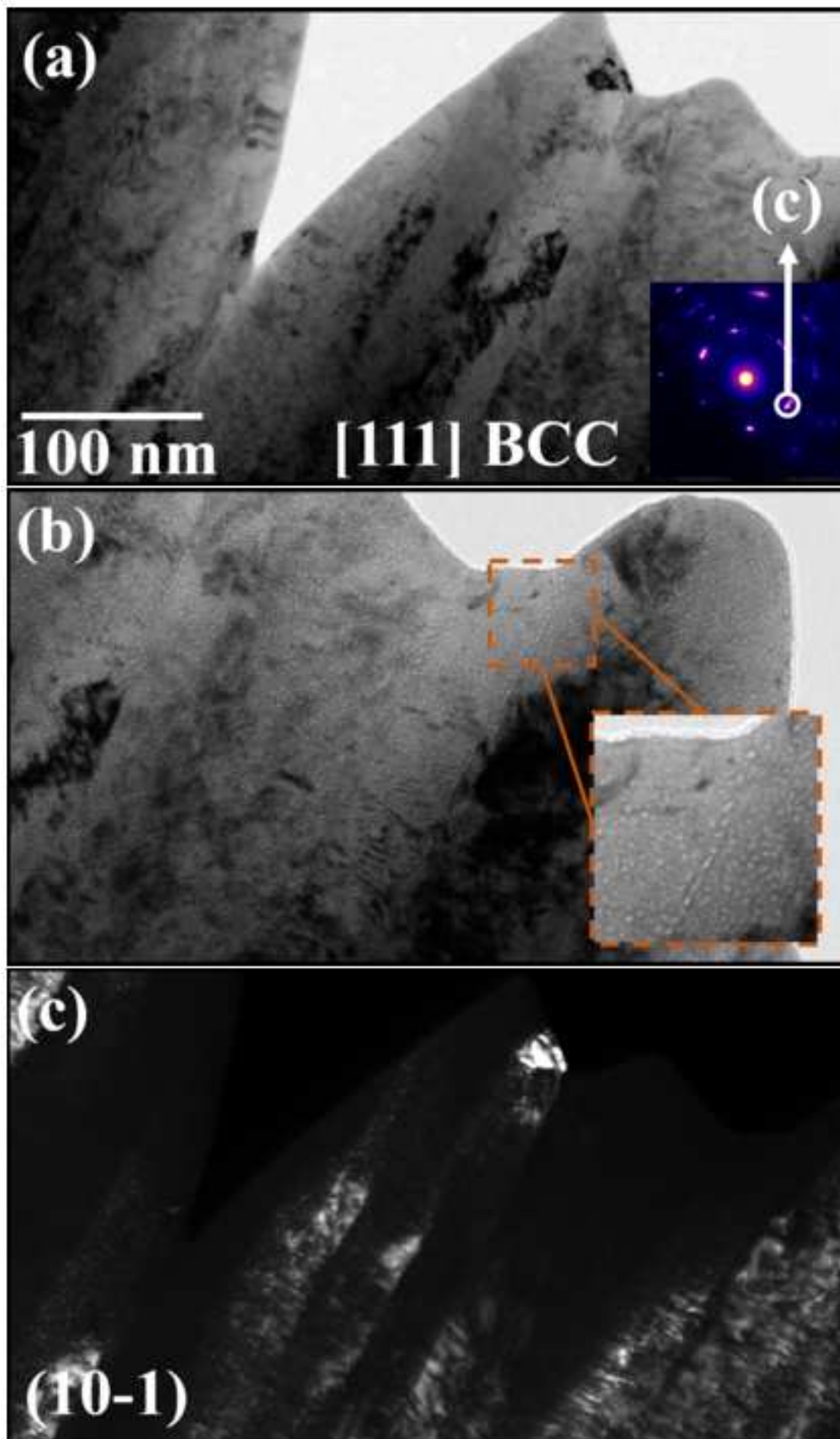


Figure 4
[Click here to download high resolution image](#)

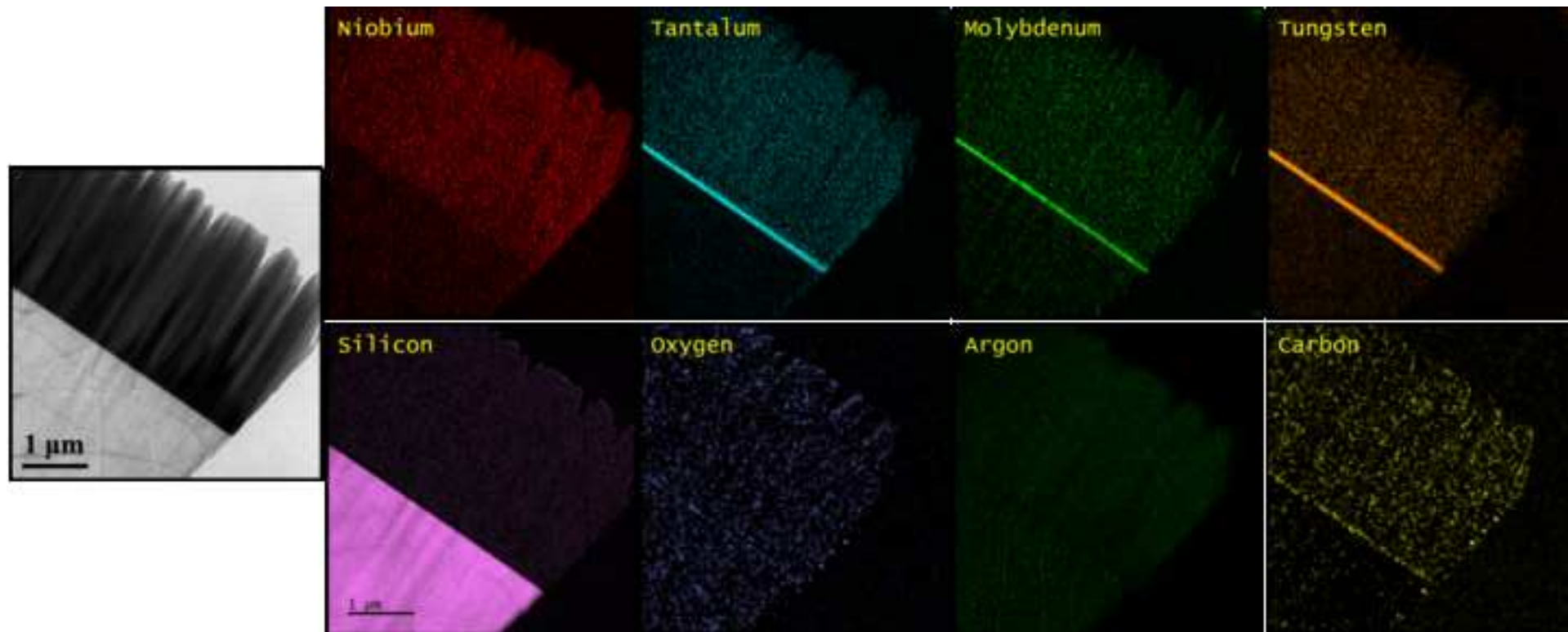


Figure 5
[Click here to download high resolution image](#)

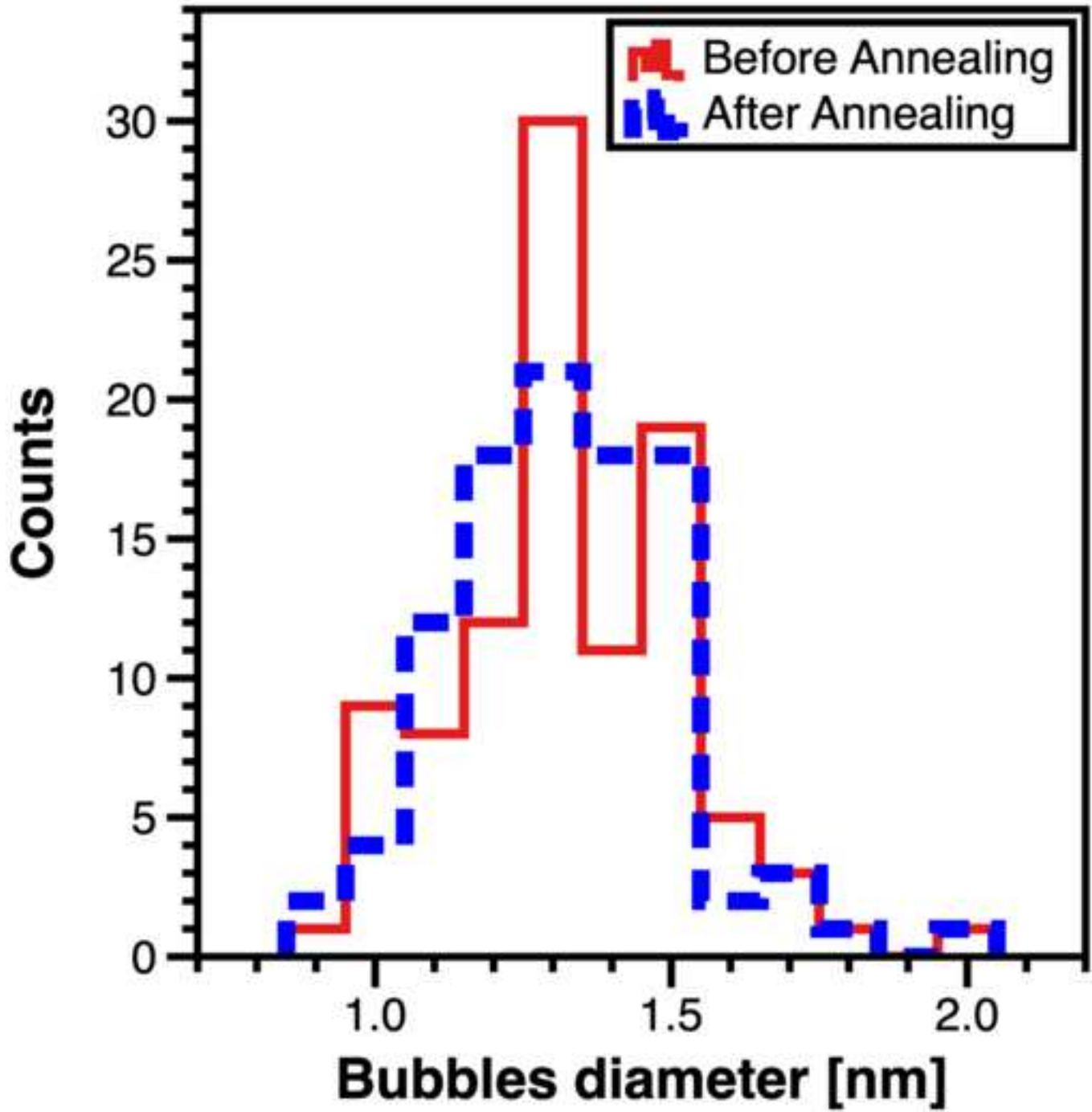


Figure 6
[Click here to download high resolution image](#)

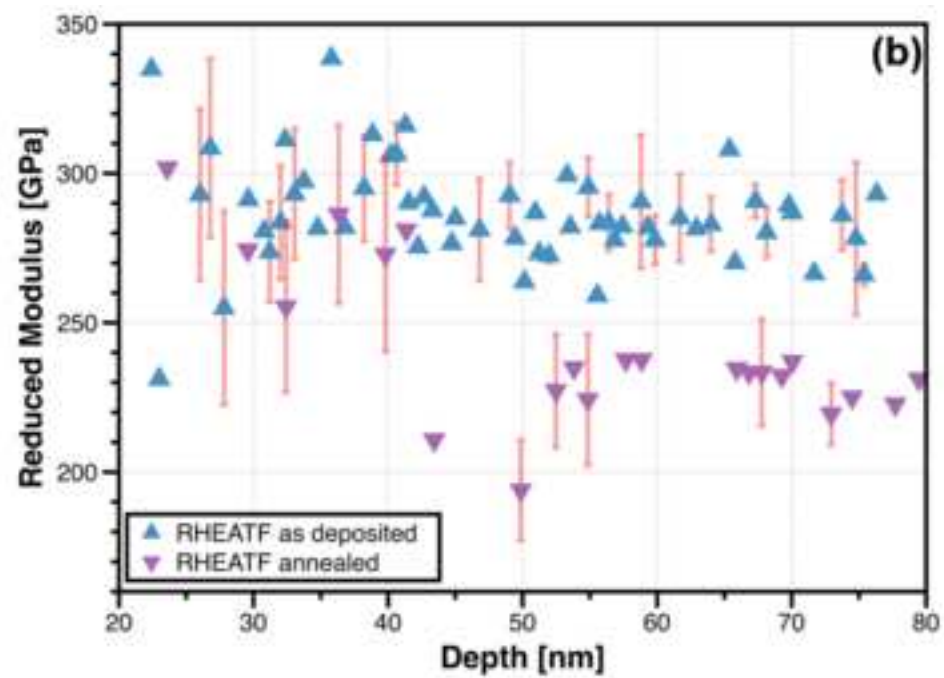
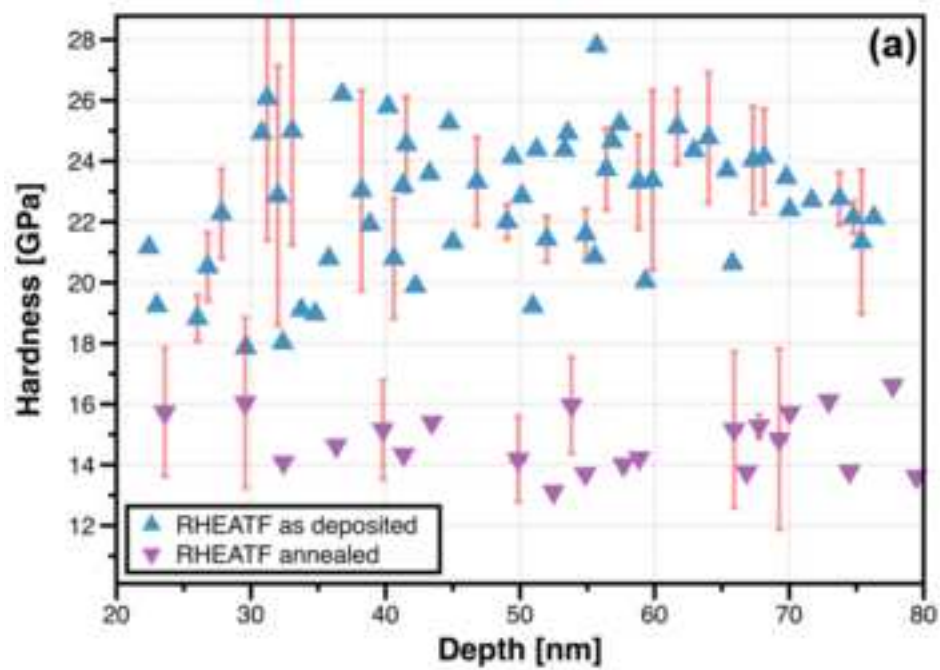


Figure 7
[Click here to download high resolution image](#)

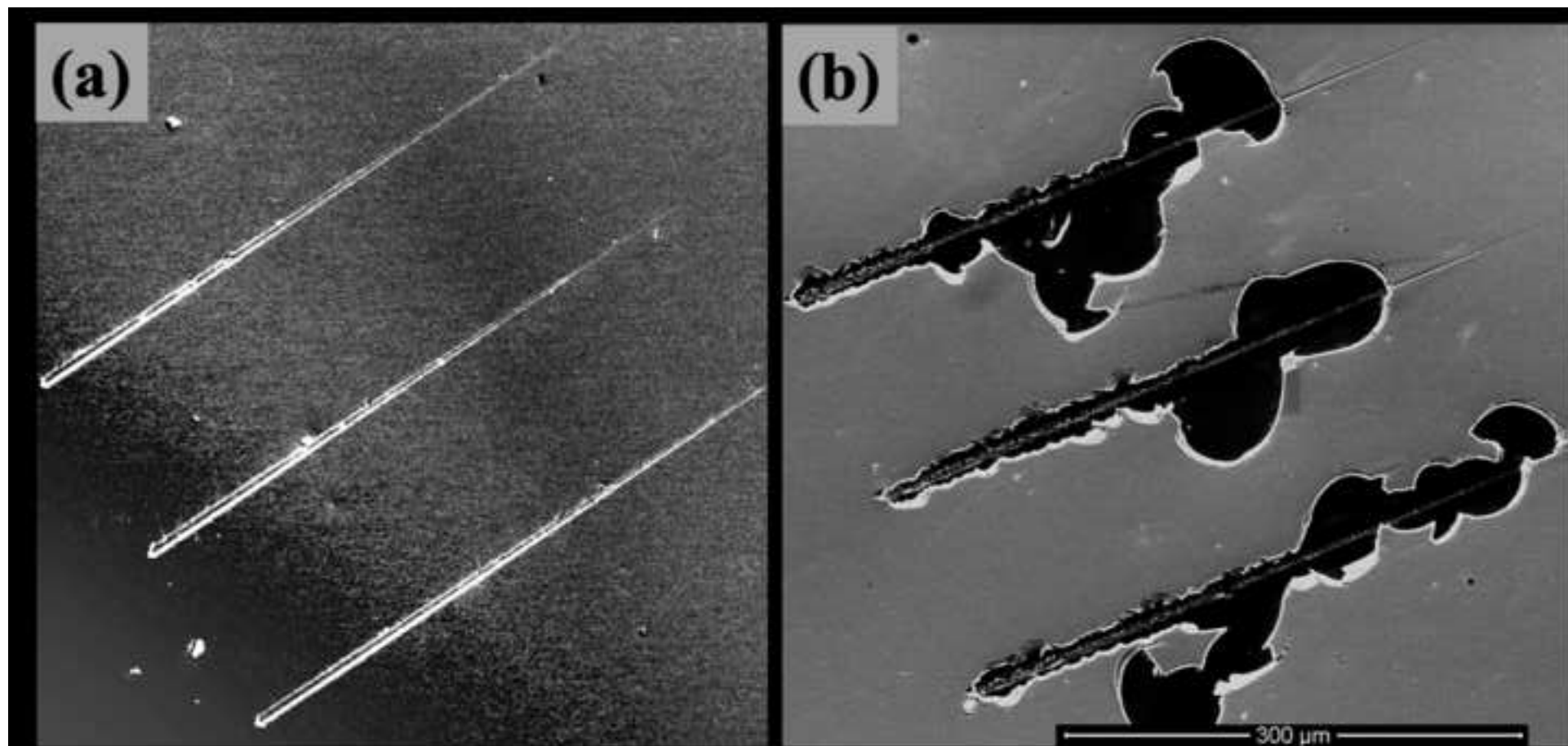


Figure 8
[Click here to download high resolution image](#)

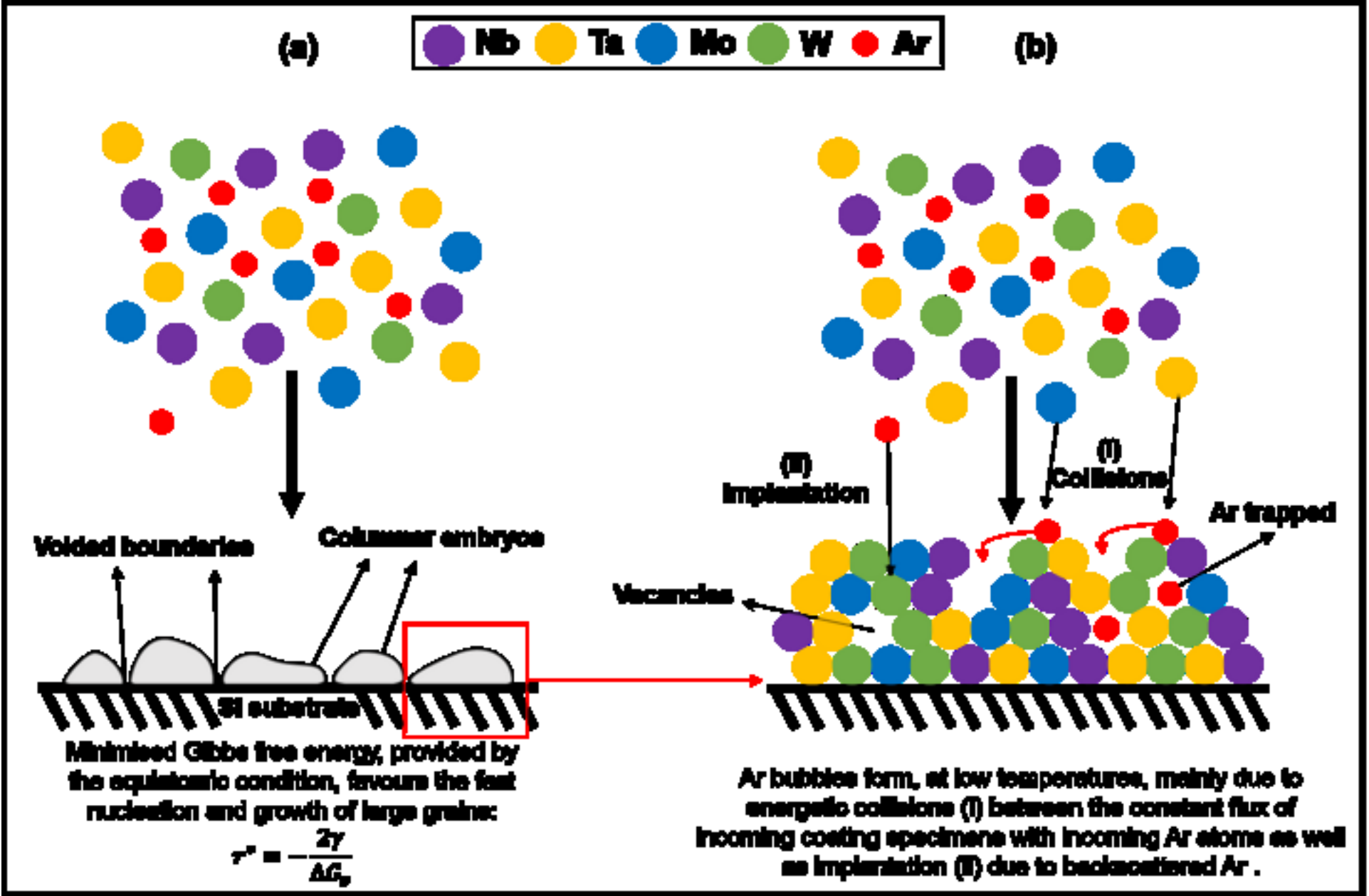
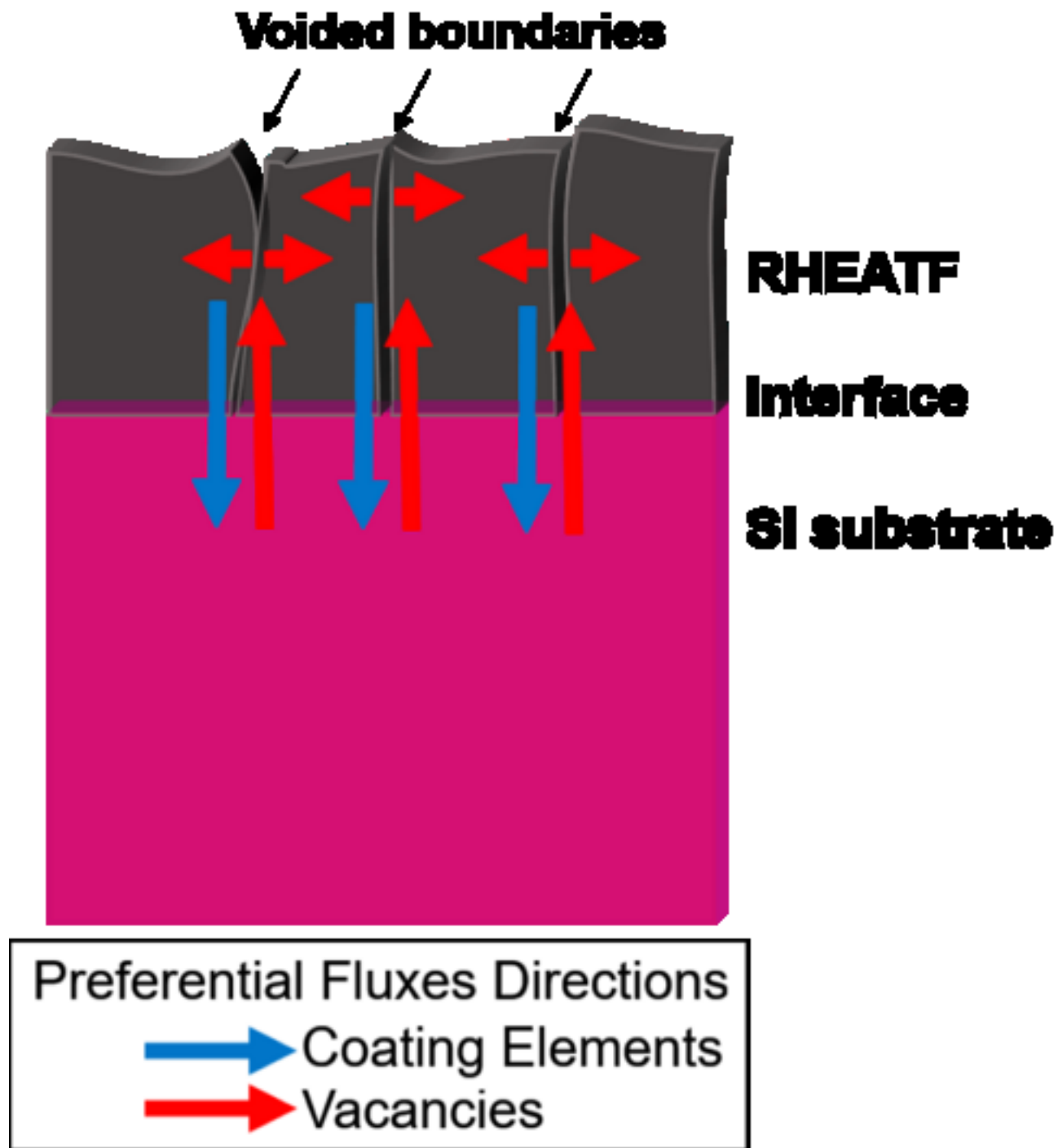


Figure 9
[Click here to download high resolution image](#)



LaTeX Source Files

[Click here to download LaTeX Source Files: latex-source-files.zip](#)

Manuscript ref: JMAD-D-18-06508R1

CRedit author statement

MAT and VMV conceptualised the idea and performed the synthesis and characterisation of the thin films reported and in this work. Both authors also were involved in data curation, visualisation and interpretation of the obtained results. MAT wrote the initial manuscript draft which was further edited and reviewed by VMV. VMV was responsible for supervision, project administration and funding acquisition.

Conflict of interest

The authors declare no conflict of interest.



Matheus A. Tunes



Vladimir V. Vishnyakov